Autophagy Cholesterol Axis Remodeling Supports Malignant Progression and Chemoresistance in Glioma

Shahla Shojaei[1], Amir Barzegar Behrooz[1], Kianoosh Naghibzadeh[1], João Basso[2,3], Javad Alizadeh[1], Tania Dehesh[4], Roham Sabei[1], Bhavya Bhushan[1], Mehdi Eshraghi[1], Simone C da Silva Rosa[1], Courtney Clark[1], Mateusz Marek Tomczyk[5], Laura Cole[5], Grant Hatch[5], Vernon W Dolinsky[5], Vinith Yathindranath[5], Donald Miller[5], Christopher Pasco[6], Sanjiv Dhingra[6], Abhay Srivastava[6], Amir Ravandi[7], Rui Vitorino[8, 9, 10], Stevan Pecic[11], Negar Azarpira[12], Mahmoud Aghaei[13], Saeid Ghavami*[14],

[1] Department of Human Anatomy and Cell Sciences, University of Manitoba, Winnipeg, MB, Canada.

[2] Faculty of Pharmacy, University of Coimbra, Coimbra, Portugal.

[3] Coimbra Chemistry Centre, Department of Chemistry, University of Coimbra, Coimbra, Portugal

[4] Department of Biostatistics and Epidemiology, School of Public Health, Kerman University of Medical Sciences, Kerman, Iran

[5] Department of Pharmacology and Therapeutics, University of Manitoba, Winnipeg, Canada

[6] Department of Physiology and Pathophysiology, University of Manitoba, Winnipeg, Manitoba, Canada.

[7] Physiology and Pathophysiology, University of Manitoba, St. Boniface Hospital Research Center, Winnipeg, Canada

[8] iBiMED-Department of Medical Sciences, University of Aveiro, Aveiro, Portugal.

[9] UnIC, Department of Surgery and Physiology, Faculty of Medicine, University of Porto, Porto, Portugal

[10] QOPNA & LAQV-REQUIMTE, Chemistry Department, University of Aveiro, Aveiro, Portugal

[11] Department of Chemistry and Biochemistry, California State University, Fullerton, CA, 92834, United States.

[12] Transplant Research Center, Shiraz University of Medical Sciences, Shiraz, Iran.

[13] Department of Clinical Biochemistry, School of Pharmacy and Pharmaceutical Sciences, Isfahan University of Medical Sciences, Isfahan, Iran.

[14] Department of Human Anatomy and Cell Science, University of Manitoba College of Medicine, Winnipeg, Manitoba, Canada; Paul Albrechtsen Research Institute, CancerCare Manitoba, University of Manitoba, Winnipeg, Manitoba, Canada; Akademia Śląska, Katowice, Poland; Children Hospital Research Institute of Manitoba, University of Manitoba, Winnipeg, Manitoba, Canada.

*:Corresponding author: Saeid Ghavami, PhD, Professor, Department of Human Anatomy and Cell Science, University of Manitoba College of Medicine, Winnipeg, Manitoba, Canada. Email: saeid.ghavami@umanitoba.ca

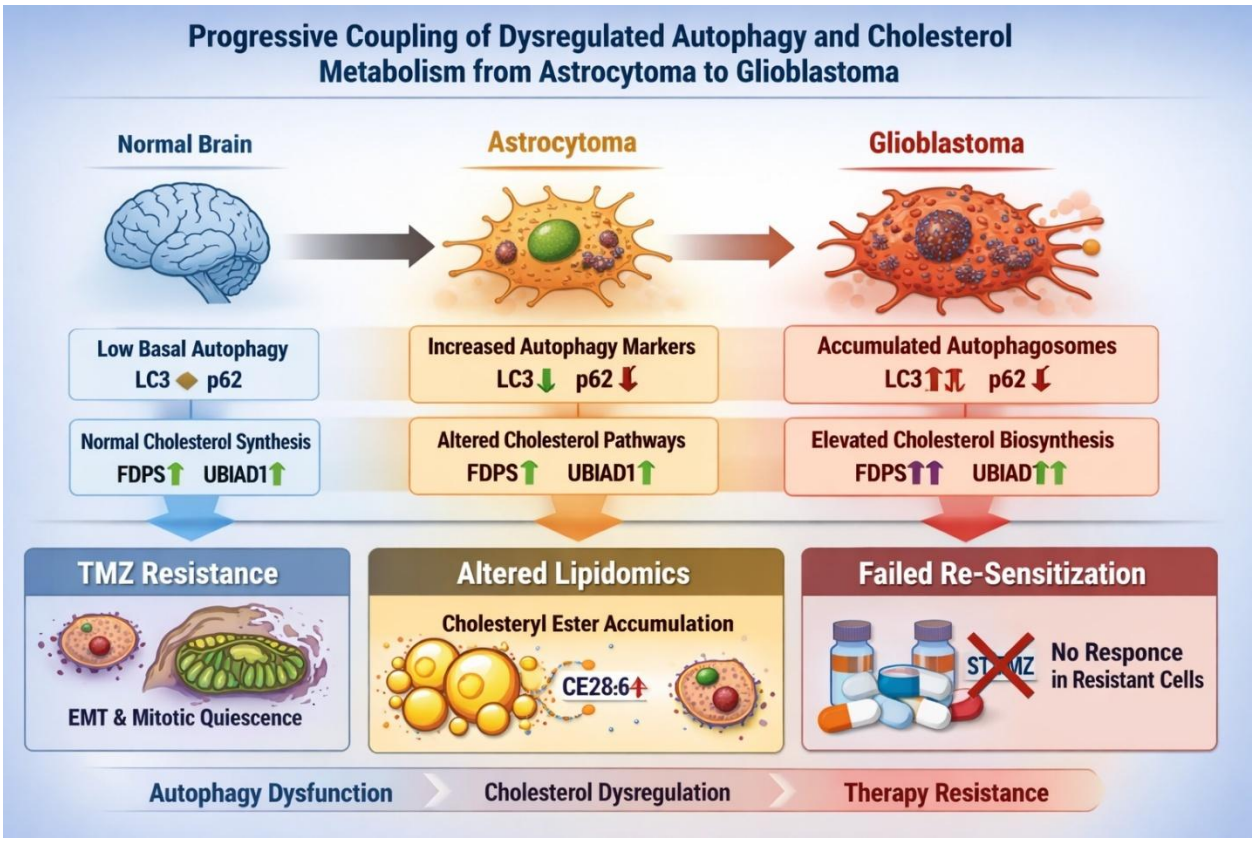

Lay Abstract: As gliomas progress from astrocytoma to glioblastoma, autophagy becomes dysregulated and cholesterol metabolism is rewired. This coordinated remodeling supports tumor survival, metabolic plasticity, and resistance to temozolomide therapy.

Abstract

Glioma progression and resistance to temozolomide (TMZ) remain major clinical challenges. Here, we investigated whether dysregulated autophagy and cholesterol metabolism are coordinately remodeled during glioma progression and TMZ resistance. Tissue microarray analysis of astrocytoma and glioblastoma specimens revealed progressive autophagosome accumulation, reflected by increased LC3β puncta, coupled with impaired autophagic flux compared with adjacent normal brain tissue. These alterations intensified with tumor grade and were associated with upregulation of farnesyl diphosphate synthase (FDPS), linking malignant progression to cholesterol pathway remodeling.

TMZ-resistant (R) glioblastoma cells exhibited epithelial-to-mesenchymal transition, mitotic quiescence, and mitochondrial remodeling consistent with a therapy-tolerant phenotype. Bioenergetic profiling demonstrated reduced respiratory reserve, diminished ATP-linked respiration, and elevated proton leak, indicating constrained metabolic flexibility. In parallel, impaired autophagy flux was associated with suppression of de novo cholesterol synthesis and transcriptional downregulation of SREBP-2 and LDL-R.

Comprehensive lipidomic profiling revealed marked cholesterol metabolic reprogramming in R cells, characterized by accumulation of specific cholesteryl esters, including CE 22:5, CE 22:6, CE 22:4, and CE 20:4, despite reduced cholesterol biosynthesis. Pharmacologic inhibition of the mevalonate pathway with simvastatin significantly altered cholesteryl ester profiles but failed to restore autophagy flux or sensitize R cells to TMZ-induced apoptosis, even under combined TMZ–simvastatin treatment.

Keywords: Temozolomide resistance; Autophagy flux blockade; Cholesterol metabolism; Cholesteryl esters; Metabolic plasticity; Mitochondrial remodeling; Glioblastoma

46

47 **Highlights**

48 • Autophagy flux blockade intensifies during progression from astrocytoma to glioblastoma

49 • Dysregulated autophagy is coupled to altered cholesterol metabolism in malignant gliomas

50 • TMZ-resistant glioblastoma cells undergo epithelial-to-mesenchymal transition and mitotic
51 quiescence

52 • Resistant cells exhibit constrained bioenergetic capacity and mitochondrial remodeling

53 • Impaired autophagy suppresses de novo cholesterol synthesis and lipid recycling

54 • Lipidomics reveals accumulation of long-chain cholesteryl esters in TMZ-resistant cells

55 • Statin-based cholesterol inhibition fails to resensitize glioblastoma cells to temozolomide

56

57

Introduction

Glioblastoma (GB) stands as one of the most formidable and therapy-resistant brain tumors in adults. Conventional treatment strategies, comprising surgical excision followed by radiotherapy and temozolomide (TMZ)-based chemotherapy, offer limited effectiveness [1, 2]. The therapeutic efficacy of TMZ is frequently compromised by the onset of resistance, reducing its long-term impact[3, 4]. Emerging research has revealed that TMZ exposure can stimulate autophagy, a cellular survival mechanism crucial to GB's resistance to treatment[5].

Autophagy serves as a paradoxical regulator in cancer, acting as both a guardian and a facilitator of tumor progression depending on cellular context [6]. This dynamic and multifaceted process influences various cancers, including glioblastoma, affecting their progression and therapeutic responses [7-9]. Autophagy dysfunction is a key driver of therapeutic resistance in GB, fueling both drug resistance and radio-resistance [10-12]. Beyond its role in treatment evasion, autophagy actively shapes GB pathophysiology by directly modulating cell survival, migration, and invasion while also rewiring metabolic networks to sustain tumor progression [12, 13].

GB cells exhibit metabolic adaptations that enhance their ability to proliferate rapidly and sustain their growth demands. One such adaptation involves reprogramming lipid metabolism, favoring de novo lipogenesis to support tumor progression [14, 15]. Recent findings indicate altered lipid homeostasis significantly drives resistance to TMZ in GB [16, 17]. Elevated intracellular cholesterol levels have been implicated in promoting TMZ resistance, highlighting the critical role of cholesterol and lipid metabolism in GB tumorigenesis [18, 19]. Villa et al. reported that, unlike astrocytes, GB cells do not rely on de novo cholesterol synthesis. Instead, they suppress key enzymes involved in cholesterol biosynthesis and predominantly acquire cholesterol from external sources[20]. Additional studies further support this observation, demonstrating that GB cells depend on low-density lipoprotein receptors (LDLR)-mediated cholesterol uptake, a process regulated by the EGFR/PI3K/Akt signaling axis [21, 22]. This metabolic shift underscores the rewiring of cholesterol metabolism in GB, enabling tumor cells to sustain their malignant behavior.

Research has demonstrated that disrupting lysosomal cholesterol efflux triggers autophagy-mediated suppression of GB cell proliferation. The opioid receptor agonists and antipsychotic drugs loperamide and pimozide drive autophagy-dependent cell death in MZ-54 GBM cells by engaging ATG5 and ATG7. These compounds hinder SMPD1, impair lysosomal activity and lead to ceramide accumulation, disrupting lysosomal degradation and its hexosyl derivatives. As a result, cholesterol becomes trapped within dysfunctional lysosomes, leading to oxidative stress-induced membrane destabilization. This process culminates in lysosomal membrane permeabilization (LMP), facilitating the release of cathepsin B (CTSB) into the cytosol, further promoting autophagy and cell death [23, 24]. The sterol regulatory element-binding protein 1 (SREBP-1) also plays a key role in regulating lipophagy to sustain cholesterol balance in GB cells. Activated in response to cholesterol scarcity, SREBP-1 enhances the expression of crucial autophagic genes such as ATG9B, ATG4A, and LC3B alongside the lysosomal cholesterol

transporter NPC2. This activation fosters the degradation of lipid droplets (LDs) via lipophagy, facilitating the breakdown of cholesteryl esters (CEs) and the mobilization of cholesterol from lysosomes, ensuring the stability of plasma membrane cholesterol levels [25]. Thus, GB progression is closely linked to the interplay between cholesterol metabolism and autophagy.

Despite extensive work on autophagy and lipid metabolism in glioblastoma, it remains unclear whether dysregulation of these pathways arises as an early feature of gliomagenesis or progressively intensifies with malignant transformation. In particular, whether autophagy–cholesterol remodeling accumulates across tumor grade—from astrocytoma to glioblastoma—and predisposes tumors to stress tolerance and therapeutic resistance has not been systematically examined. Moreover, while autophagy is frequently described as "activated" in GB [26-28], increasing evidence suggests that high-grade tumors may instead exhibit a state of autophagy flux blockade, characterized by autophagosome accumulation without efficient lysosomal degradation. Such a state could fundamentally alter lipid handling and metabolic feedback regulation.

Importantly, impaired autophagy flux is predicted to disrupt endogenous lipid recycling [29-31], raising the possibility that metabolic adaptations in resistant glioblastoma cells may not be reversible by simple replenishment or inhibition of cholesterol biosynthesis alone. Whether pharmacologic modulation of cholesterol availability—through exogenous lipid delivery or HMG-CoA reductase inhibition—can overcome resistance in the context of autophagy flux blockade remains unresolved. Addressing this question is essential, as it challenges prevailing assumptions that correcting metabolic deficits is sufficient to restore chemosensitivity.

In this study, we systematically dissect the relationship between autophagy dysregulation, cholesterol metabolism, and metabolic reprogramming across glioma progression and in the setting of temozolomide resistance. Using patient-derived tissue microarrays, resistant glioblastoma models, lipidomics, and mitochondrial functional analyses, we demonstrate that autophagy flux blockade and cholesterol pathway remodeling intensify with tumor grade and stabilize a stress-tolerant, therapy-resistant phenotype. We further show that pharmacologic modulation of cholesterol metabolism fails to restore chemosensitivity once this adaptive program is established. Together, these findings define an autophagy–cholesterol axis as a central organizing principle of malignant progression and chemoresistance in glioblastoma.

MATERIALS AND METHODS

Cell Culture

All experiments were performed using the U251-mKate human glioblastoma cell line, originally developed by Dr. Marcel Bally (Experimental Therapeutics, British Columbia Cancer Agency, Vancouver, BC, Canada). Cells were maintained in high-glucose Dulbecco's modified Eagle's medium (DMEM; 4 mg/mL glucose; Corning, 50-003-PB) supplemented with 10% fetal bovine serum (FBS; Gibco™, 16000044) and 1% penicillin–streptomycin. Cultures were maintained under standard humidified conditions at 37 °C with 5% CO_2 and routinely monitored to ensure exponential growth and absence of contamination prior to experimentation.

Immunohistochemistry for Autophagy and Cholesterol Metabolism Markers

Tissue microarray (TMA) sections containing astrocytoma, glioblastoma, and matched adjacent non-neoplastic brain tissues were used for immunohistochemical analysis of autophagy and cholesterol metabolism–associated proteins. Formalin-fixed, paraffin-embedded tissue sections (4 µm thickness) were deparaffinized in xylene and rehydrated through a graded ethanol series to distilled water.

Antigen retrieval was performed by heating sections in citrate buffer (10 mM sodium citrate, pH 6.0) using a pressure cooker or microwave for 15–20 min, followed by gradual cooling to room temperature. Endogenous peroxidase activity was quenched by incubating sections in 3% hydrogen peroxide for 10 min. Non-specific binding was blocked by incubation with 5% normal serum (matched to the secondary antibody host species) for 30 min at room temperature.

Sections were incubated overnight at 4 °C with the following primary antibodies diluted in antibody diluent: anti-LC3β (for autophagosome detection), anti-p62/SQSTM1 (for assessment of autophagic flux), anti-FDPS (ab153805, Abcam; 1:200 dilution), and anti-UBIAD1 (NBP2-82046, Novus Biologicals; 1:200 dilution). Each marker was stained on serial sections under identical conditions.

After washing in phosphate-buffered saline (PBS), sections were incubated with appropriate HRP-conjugated secondary antibodies for 30 min at room temperature. Immunoreactivity was visualized using 3,3′-diaminobenzidine (DAB) as chromogen, followed by counterstaining with hematoxylin. Sections were dehydrated, cleared, and mounted using permanent mounting medium.

Immunostained slides were digitally scanned or examined under light microscopy. Cytosolic puncta formation for LC3β and p62 was evaluated as a surrogate for autophagosome abundance and autophagic flux, respectively. FDPS and UBIAD1 expression were assessed based on cytoplasmic staining intensity. Staining intensity and puncta density were semi-quantitatively scored by at least two independent observers blinded to clinicopathological data. Discrepancies were resolved by joint review. Quantitative and categorical scoring results were used for downstream statistical and correlation analyses.

Generation of a Resistant GBM Cell Line

U251-mKate cells were cultured in T75 tissue culture flasks in a complete medium containing high glucose DMEM, 10% FBS (Gibco, 10437-036), and 1% penicillin-streptomycin (Gibco, 15140122) and incubated at 37°C, 5% CO_2, in a humidified incubator (Thermo Fischer Scientific, USA). A pulsed-selection strategy was chosen to make a clinically relevant chemoresistant model [32]. Once cells reached 70% confluence, they were treated with 100 µM TMZ (Sigma Aldrich, T2577) over three weeks, followed by four weeks of TMZ-free medium for recovery. Cells were cultured in complete medium with 250 µM TMZ for three weeks, followed by another four weeks with TMZ-free medium. The final population of U251-mKate cells resistant to 250 µM TMZ was selected and cultured in a complete medium without TMZ for four weeks.

Immunoblotting

Protein expression was analyzed by Western blotting, using GAPDH and Ponceau S staining as loading and transfer controls. Cells were lysed in ice-cold lysis buffer containing 20 mM Tris–HCl (pH 7.5), 0.5% Nonidet P-40, 0.5 mM phenylmethylsulfonyl fluoride (PMSF; Sigma-Aldrich,

P7626), 100 μM β-glycerol 3-phosphate (Sigma-Aldrich, 50020), and 0.5% protease and phosphatase inhibitor cocktail (Sigma-Aldrich, PPC1010). Lysates were clarified by centrifugation at 10,000 × g for 10 min at 4 °C, and supernatants were collected for analysis. Protein concentrations were determined using the Lowry assay. Equal amounts of protein were resolved by SDS–polyacrylamide gel electrophoresis and transferred onto polyvinylidene difluoride (PVDF) membranes. Membranes were blocked with 5% skim milk in Tris-buffered saline containing 0.1% Tween-20 (TBST) for 1 h at room temperature, followed by incubation with primary antibodies diluted in 1% skim milk in TBST overnight at 4 °C. After washing, membranes were incubated with horseradish peroxidase (HRP)–conjugated secondary antibodies for 2 h at room temperature. Immunoreactive bands were detected using enhanced chemiluminescence (ECL; Amersham-Pharmacia Biotech) and visualized using a Bio-Rad imaging system. Band intensities were quantified by densitometric analysis using AlphaEase FC software [33, 34].

Transmission Electron Microscopy (TEM)

Autophagic structures and mitochondrial ultrastructure were examined using transmission electron microscopy (TEM). Cells were cultured in 100-mm dishes in Dulbecco's modified Eagle's medium (DMEM) supplemented with 10% fetal bovine serum and 1% penicillin–streptomycin under standard humidified incubator conditions (37 °C, 5% CO_2). Cells were harvested and immediately fixed in Karnovsky's fixative (Sigma-Aldrich, SBR00124) for 1 h at 4 °C. Following fixation, cell pellets were resuspended in 5% sucrose prepared in 0.1 M Sørensen's phosphate buffer and incubated overnight at 4 °C. Samples were then pelleted and post-fixed with 1% osmium tetroxide in 0.1 M Sørensen's phosphate buffer for 2 h at room temperature. Cells were subsequently dehydrated through a graded ethanol series and embedded in Embed 812 resin (Sigma-Aldrich, 45347). Ultrathin sections (~200 nm) were cut using an ultramicrotome and mounted on copper grids. Sections were stained with uranyl acetate followed by lead nitrate for contrast enhancement. Ultrastructural imaging was performed using a Philips CM10 transmission electron microscope, allowing detailed visualization of autophagosomes, mitochondrial morphology, and intracellular membrane organization [34].

Cell Proliferation by Trypan Blue Exclusion and Direct Cell Counting

Baseline proliferation of U251 glioblastoma NR and R cells was quantified by direct cell counting using Trypan Blue exclusion. Cells were maintained in high-glucose DMEM supplemented with 10% FBS and 1% penicillin/streptomycin. To ensure comparable starting confluence between groups, NR and R cells were seeded at equal densities (50,000 cells/mL) in tissue-culture plates and allowed to grow under standard conditions (37°C, 5% CO_2).

At the indicated time points (72h), both floating and adherent cells were collected. Culture supernatants were retained, adherent cells were detached using trypsin–EDTA, and the fractions were combined to avoid underestimation of cell loss. Cell suspensions were mixed 1:1 with 0.4% Trypan Blue, and viable (Trypan Blue–negative) and non-viable (Trypan Blue–positive) cells were counted using a hemocytometer (or an automated cell counter). Proliferation was expressed as the total number of viable cells per well at each time point. Viability (%) was calculated as: (viable cells / total cells) × 100, and fold-change in viable cell number relative to baseline (time 0) was reported where indicated.

219 **Flow Cytometry/Cell Cycle Analysis**

220 U251 glioblastoma cells were seeded in 12-well plates at a density of 50,000 cells/well for TMZ-
221 non-resistant (NR) cells and 75,000 cells/well for TMZ-resistant (R) cells and allowed to grow to
222 approximately 60% confluence. Cells were then treated with temozolomide (TMZ; 250 μM) for
223 48 h. Following treatment, cells were detached using EDTA buffer, collected by centrifugation at
224 300 × g for 10 min, and washed once with phosphate-buffered saline (PBS). Cell pellets were
225 resuspended in hypotonic propidium iodide (PI) lysis buffer containing 0.01% Triton X-100, 1%
226 sodium citrate, and 40 μg/mL PI, and incubated for 30 min at room temperature in the dark.
227 DNA content was analyzed by flow cytometry using a Beckman Coulter CytoFLEX LX flow
228 cytometer equipped with a 488-nm laser and a 610/20 band-pass filter. Cell populations
229 corresponding to sub-G0/G1 (apoptotic), G0/G1, S, and G2/M phases were quantified based on
230 DNA content [35].

231 **Measurement of Mitochondrial Respiration**

232 Mitochondrial respiration was assessed by measuring the oxygen consumption rate (OCR) using
233 an Agilent Seahorse XFe24 extracellular flux analyzer. NR and R glioblastoma cells were seeded
234 at a density of approximately 0.3×10^6 cells per well in XF24 cell culture microplates in complete
235 growth medium and allowed to adhere overnight. On the day of the assay, cells were washed twice
236 and the medium was replaced with Seahorse XF Base Minimal DMEM supplemented with
237 glucose, L-glutamine, and sodium pyruvate (Agilent Technologies, #103334-100). Cells were then
238 incubated at 37 °C in a non-CO_2 incubator for 1 h prior to analysis. Baseline OCR was recorded,
239 followed by sequential injections of mitochondrial modulators to interrogate respiratory
240 parameters. Proton leak–associated respiration was measured following the injection of
241 oligomycin (1 μM). Maximal respiratory capacity was determined by addition of the mitochondrial
242 uncoupler FCCP (2 μM). Non-mitochondrial respiration was assessed after combined injection of
243 rotenone (1 μM) and antimycin A (1 μM). OCR data were normalized to live cell number by
244 staining individual wells with Hoechst 33342 (Invitrogen, #R37605) and quantifying nuclear
245 signal using a Cytation 5 imaging system (BioTek). Maximal respiration was calculated by
246 subtracting non-mitochondrial OCR from FCCP-stimulated OCR. Spare respiratory capacity was
247 determined by subtracting baseline OCR from FCCP-stimulated OCR. ATP-linked respiration was
248 calculated by subtracting oligomycin-treated OCR from baseline OCR, and proton leak was
249 calculated by subtracting non-mitochondrial OCR from oligomycin-treated OCR. Data are
250 presented as pmol O_2 per minute per cell.

251 **Gene Expression Analysis**

252 Total RNA was extracted according to the manufacturer's instructions using the PureLink RNA
253 Mini Kit (Invitrogen, #12183018A). RNA concentration and purity were assessed, and 500 ng of
254 total RNA was reverse-transcribed into complementary DNA (cDNA) using the LunaScript RT
255 SuperMix Kit (New England Biolabs, #E3010L). Quantitative real-time PCR (qPCR) was
256 performed using the Luna Universal qPCR Master Mix (New England Biolabs, #M3003X) with
257 10 ng cDNA per well in a 96-well plate format on a CFX96 Real-Time PCR Detection System
258 (Bio-Rad).

Gene expression of LDL receptor (LDL-R) and sterol regulatory element-binding protein 2 (SREBP-2) was quantified using the following primers: LDL-R forward, 5′-CCCGACCCCTACCCACTT-3′; LDL-R reverse, 5′-AATAACACAAATGCCAAATGTACACA-3′; SREBP-2 forward, 5′-GACGCCAAGATGCACAAGTC-3′; SREBP-2 reverse, 5′-ACCAGACTGCCTAGGTCGAT-3′.

For normalization, β-ACTIN (forward, 5′-CACCATTGGCAATGAGCGGTT-3′; reverse, 5′-AGGTCTTTGCGGATGTCCACGT-3′), EIF2α (forward, 5′-CGAAACACTGTCTCTCAGTCAA-3′; reverse, 5′-CCAGTTGCTGCTTGTTCTTTC-3′), and 18S rRNA (forward, 5′-GCAGAATCCACGCCAGTACAAG-3′; reverse, 5′-GCTTGTTGTCCAGACCATTGGC-3′) were used as reference genes. Gene expression levels were normalized using the geometric mean of β-ACTIN, EIF2α, and 18S.

Primer specificity was verified by in silico PCR using the ENCODE UCSC Genome Browser and experimentally confirmed by electrophoresis of PCR products on a 1% agarose gel prepared in 1× Tris-Acetate-EDTA (TAE) buffer (MP Biomedicals, #TAW50X01) at 100 V for 45 min.

MitoView Live-Cell Imaging

Live-cell mitochondrial imaging was performed using MitoView™ Green (Biotium, #70054) to assess mitochondrial morphology and network organization, and Hoechst 33342 (Biotium, #33342) to visualize cell nuclei. NR and R glioblastoma cells were cultured on glass-bottom dishes (or tissue-culture–treated plates) under standard growth conditions. Cells were incubated with MitoView Green at a final concentration of 100 nM and Hoechst 33342 at 5 μM, prepared in pre-warmed complete culture medium. Staining was performed for 15–30 min at 37 °C in a humidified incubator protected from light. Following incubation, cells were gently washed with pre-warmed phosphate-buffered saline to remove excess dye and maintained in fresh, phenol red–free medium for imaging. Live-cell fluorescence imaging was carried out immediately using an epifluorescence or confocal microscope equipped with appropriate excitation/emission filters. Imaging parameters were kept constant across all experimental conditions to allow direct comparison of mitochondrial morphology between NR and R cells.

Preparation and Characterization of Cholesterol-Containing Lipid Nanoparticles (LNPs)

Cholesterol-containing lipid nanoparticles (LNPs) were prepared using a microfluidic mixing approach. Lipid components, including 1,2-dioleoyl-sn-glycero-3-phosphocholine (DOPC), 1,2-distearoyl-sn-glycero-3-phosphocholine (DSPC), cholesterol, 1,2-dimyristoyl-rac-glycero-3-methoxypolyethylene glycol-2000 (DMG-PEG), and the fluorescent lipid tracer DiO, were obtained from Avanti Polar Lipids/Sigma-Aldrich (St. Louis, MO, USA). Lipids were dissolved in ethanol at a molar ratio (%) of 50:10:38:1.5:0.5 (DOPC:DSPC:cholesterol:DMG-PEG:DiO), and the total lipid concentration of the organic phase was maintained at 10 mg/mL.

LNPs were formed by rapidly mixing 0.5 mL of the ethanol-based lipid solution with 1.5 mL of aqueous phosphate-buffered saline (PBS, pH 7.4) using a herringbone-patterned microfluidic cartridge on a NanoAssemblr Benchtop instrument (Precision NanoSystems, Vancouver, BC, Canada). Microfluidic assembly was performed at a flow rate ratio (FRR) of 1:3 (organic

phase:aqueous phase) and a total flow rate (TFR) of 12 mL/min, enabling controlled and reproducible nanoparticle self-assembly.

Following formulation, LNP suspensions were purified to remove residual ethanol by centrifugal filtration using a 10 kDa molecular weight cut-off membrane at 2000 × g with PBS (pH 7.4). Purified LNPs were concentrated to a final volume of 0.5 mL, corresponding to a lipid concentration of 10 mg/mL, and stored at 4 °C until use.

The hydrodynamic diameter, polydispersity index (PDI), and surface charge (zeta potential) of the LNPs were determined by dynamic light scattering using a ZetaPALS analyzer (Brookhaven Instruments, NY, USA). For measurements, LNPs were diluted in PBS (pH 7.4) to a final lipid concentration of 20 µg/mL. The formulated LNPs exhibited a mean hydrodynamic diameter of 65.3 ± 1.4 nm, a near-neutral zeta potential (−0.68 ± 2.3 mV), and a PDI of 0.151 ± 0.038, indicating a stable and monodisperse nanoparticle population under physiological conditions.

Phase Contrast

Bright-field images were acquired using an Axio Observer microscope (ZEISS, Oberkochen, Germany) equipped with 20× and 50× objective lenses. Image processing, including background subtraction, scale bar calibration, and quantitative analysis, was performed using Fiji (ImageJ) and ZEN 2.3 Pro software (ZEISS).

Cholesterol Mass Measurement

NR and R glioblastoma cells were cultured in cholesterol-free medium and harvested at 24, 48, and 72 h. Cellular cholesterol content was quantified according to the manufacturer's instructions using the Amplex Red Cholesterol Assay Kit (Invitrogen, Thermo Fisher Scientific, Toronto, Canada), as previously described [36, 37]. Cholesterol levels were normalized to total cellular protein content.

De Novo Cholesterol Biosynthesis and Cholesterol Esterification

De novo cholesterol biosynthesis and cholesterol esterification were assessed using a modified Mokashi protocol [37]. Briefly, NR and R cells were cultured in cholesterol-free medium supplemented with ITS (insulin–transferrin–selenium) for 24, 48, and 72 h. Cells were then incubated in serum-free DMEM containing 2 µCi [^{14}C]-acetate per 2 mL dish for the indicated time periods. Following incubation, cells were harvested and washed twice with ice-cold PBS (pH 7.4). Total lipids were extracted as described previously [38], and incorporation of radiolabeled acetate into free cholesterol and cholesteryl esters was quantified and normalized to total protein content, as previously reported [39].

MTT Cell Viability Assay

Cell viability was assessed using the MTT assay as previously described [35], with modifications to evaluate the effects of LNP and TMZ in NR and R U251 glioblastoma cells, as well as in primary astrocytes.

Cells were cultured in high-glucose DMEM supplemented with 10% fetal bovine serum and 1% penicillin/streptomycin and seeded into 96-well plates (Corning, #353072). To achieve comparable baseline confluence, NR cells were seeded at 2,300 cells/well and R cells at 3,100

cells/well in a final volume of 200 µL per well. Cells were allowed to adhere overnight and treated once cultures reached approximately 50% confluence. Cells were treated with LNP (5, 10, 25, or 100 µg/mL), TMZ (100 or 200 µM), or their combinations for 72 h. Control wells received vehicle only. All treatments were prepared in complete DMEM containing 10% FBS. Primary astrocytes were treated in parallel to assess CE-NP toxicity in non-tumor cells. Following treatment, MTT reagent (20 µL of 5 mg/mL stock solution in PBS; final concentration 0.5 mg/mL) was added directly to each well and plates were incubated for 3 h at 37 °C in 5% CO_2, protected from light. The culture medium was then carefully aspirated, and formazan crystals were solubilized by adding 200 µL dimethyl sulfoxide (DMSO) per well with gentle mixing. Absorbance was measured immediately at 570 nm using a Synergy H1 microplate reader (BioTek). Background absorbance from media-only wells was subtracted. Cell viability was calculated as a percentage relative to untreated control cells using the formula: (OD_{570} treated / OD_{570} control) × 100. Data were analyzed using Prism software, and statistical significance was determined by two-way ANOVA.

Liquid Chromatography-Mass Spectrometry (LC-MS) for Lipidomics Analysis of Ceramide Species

Lipids were extracted from U251 GB cells (NR, R, NR-BCL2L13-KD, R-BCL2L13-KD) using a chloroform:methanol (2:1, v:v) mixture. Cells grown to confluence were collected, sonicated, and centrifuged (1000 g, 10 min). The supernatant was mixed with the internal standard (ISTD), vortexed, and centrifuged (3500 rpm, 5 min). The lower phase was dried under N_2 gas and reconstituted in water-saturated butanol, followed by methanol with 10 mM ammonium formate. After centrifugation (10,000g, 10 min), lipids were analyzed by LC-MS. Separation was performed on a Zorbax C18 column using a linear gradient of mobile phases A and B, both containing 10 mM ammonium formate. The elution program involved increasing from 0% to 100% mobile phase B over 8 min, with re-equilibration to starting conditions before the next injection. Diacylglycerol and triacylglycerol species were separated isocratically at 100 µl/min. The column was maintained at 50°C, and the injection volume was 5 µl.

Lipids eluted from the HPLC system were introduced into the AbSciex 4000 QTRAP triple quadrupole linear hybrid mass spectrometer. The mass spectrometer was operated in scheduled Multiple Reaction Monitoring (MRM) mode. Unique lipids (322) spanning 25 lipid classes/subclasses were screened for targeted semi-quantification. All lipid species other than fatty acids were scanned in positive electrospray ionization mode [ESI+]. The individual lipids in each lipid class were identified by lipid class-specific precursor ions or neutral losses. Lipids were then quantified by comparing the deisotoped lipid peak areas against those of the class-specific ISTDs added before lipid extraction. The total carbon number of the fatty acids represented lipids. In ESI+ mode, the instrument settings were optimized as follows: curtain gas (psi), 26; collision gas (nitrogen), medium; ion spray voltage (V), 5500; temperature (°C), 500.0; ion source gas 1 (psi), 40.0; ion and source gas 2 (psi), 30.0. The MRM detection window was fixed between 45 s and 90 s depending upon the chromatographic peak width of the lipid class. Isobaric species within the same class, such as PC(O) and PC(P), exhibited clear separation in this method. Also, molecular species within the same lipid class, which differ only in the number of double bonds, were well separated chromatographically. All analyses were performed with R software (version 4.1.1). Limma, pheatmap, and ggplot2 packages were used.

SMILES Code Retrieval and Annotation

SMILES (Simplified Molecular Input Line Entry System) representations for lipid species identified by LC–MS–based lipidomics were retrieved from the Human Metabolome Database (HMDB; https://hmdb.ca). For each statistically significant lipid, SMILES annotations were cross-validated against LC–MS fragmentation patterns to confirm consistency with experimentally determined head groups, acyl chain composition, and degrees of unsaturation. When multiple structural isomers were available, the canonical SMILES format was selected to ensure uniform representation. The validated SMILES codes were subsequently used for downstream cheminformatics and pathway analyses.

Statistics and reproducibility

All experiments were conducted in triplicate, with three independent repeats. Data are presented as mean ± standard deviation. Statistical significance was determined using a two-tailed t-test or one-way/two-way ANOVA with Tukey's post hoc test for multiple comparisons, considering p-values ≤ 0.05 as significant. Lipid classification and annotation were performed using the LIPIDMAPS database. Lipidomic data were analyzed with MetaboAnalyst 5.0, including hierarchical clustering, principal component analysis (PCA), and partial least squares discriminant analysis (PLSDA) to identify differential lipids. Spearman's rank correlation analysis was performed to assess associations between behavioral performance in the novel object place (NOP) and novel object recognition (NOR) tests and mitochondrial and mitophagosome numbers, as well as BCL2 family protein expression levels, in the cortex and hippocampus of female and male 3xTg-AD mice. All statistical tests were two-tailed, and a P value < 0.05 was considered statistically significant.

Results

Progressive Coupling of Dysregulated Autophagy and Cholesterol Metabolism from Astrocytoma to Glioblastoma

To investigate whether autophagy and cholesterol metabolism are coordinately altered during glioma progression, we performed a comprehensive tissue microarray–based analysis of autophagy-associated markers (LC3β and p62/SQSTM1) and cholesterol/isoprenoid biosynthesis enzymes (FDPS and UBIAD1) in astrocytoma and glioblastoma specimens, together with matched adjacent non-neoplastic brain tissues.

Autophagosome-associated LC3β was assessed by quantification of cytosolic LC3 puncta, which reflect steady-state autophagosome abundance [23, 36, 40-42]. Adjacent normal brain tissues exhibited low LC3 puncta density, consistent with basal autophagy. In contrast, both astrocytoma and glioblastoma specimens demonstrated significantly increased LC3β puncta, with glioblastoma displaying a markedly higher puncta burden than astrocytoma, indicating subtype- and grade-dependent autophagosome accumulation (**Figure 1A, Table 1**). Overall, strong LC3β puncta expression was observed in 63 of 68 tumor cores (92.6%), with 67 of 68 tumors (98.5%) showing LC3β positivity, whereas normal tissues showed predominantly weak or moderate puncta intensity ($P < 0.0001$; **Table 1**).

We next evaluated p62/SQSTM1, a selective autophagy adaptor that binds LC3β and is degraded during effective autophagic flux [3]. Immunohistochemical analysis revealed absent or weak p62 puncta in the majority of tumor specimens (54 of 67; 80.6%), with no significant difference in

422 overall p62 positivity between tumor and normal tissues (P = 0.499; **Figure 1B, Table 1**).
423 Integration of LC3β and p62 puncta using established criteria allowed inference of relative
424 autophagy states [42]. Among tumor tissues, the predominant pattern was autophagosome
425 accumulation (49 of 67; 73.1%), whereas only a small fraction (5 of 67; 7.5%) exhibited features
426 consistent with relatively preserved autophagic flux (**Table 1**). In contrast, normal brain tissues
427 more frequently demonstrated effective autophagic flux (6 of 10; 60%), confirming a tumor-
428 associated shift toward autophagosome accumulation (P < 0.0001; **Table 1**).

429 Given the emerging links between autophagy and lipid metabolism in cancer, we examined the
430 expression of FDPS and UBIAD1, two key enzymes involved in cholesterol and isoprenoid
431 biosynthesis [43-45]. FDPS expression was significantly elevated in tumor tissues (51 of 68;
432 75.0%) compared with normal brain tissues (3 of 10; 30.0%) (P = 0.007; **Figure 1C, Table 1**),
433 implicating FDPS upregulation in glioma-associated metabolic reprogramming. In contrast,
434 UBIAD1 expression was detected in most tumors (58 of 68; 85.3%) but did not differ significantly
435 between tumor and normal tissues (P = 0.344; **Figure 1D, Table 1**).

436 Subtype-specific analyses further demonstrated that astrocytoma and glioblastoma differ in the
437 magnitude of these alterations. Astrocytomas showed significantly increased LC3β puncta, FDPS
438 expression, and autophagosome accumulation relative to normal tissues, but retained greater
439 heterogeneity in autophagy states (**Table 2**). Glioblastomas, by contrast, uniformly exhibited
440 strong LC3β puncta and were overwhelmingly classified as autophagosome-accumulating, with
441 significantly higher FDPS expression than normal tissues (**Figure 1A–D, Table 3**). UBIAD1
442 expression remained largely independent of tumor subtype.

443 Correlation analyses revealed coordinated relationships among autophagy-related markers,
444 cholesterol metabolism enzymes, and clinicopathological variables. Spearman correlation matrices
445 demonstrated strong positive associations between LC3β puncta and inferred autophagy activity
446 across all tumors and within astrocytoma and glioblastoma subgroups (**Figure 1E, Table 1**). p62
447 puncta showed a consistent inverse correlation with autophagic flux activity across all tumor
448 subtypes, including glioblastoma (r = −0.739, P < 0.0001), supporting impaired autophagic
449 clearance. LC3β puncta were positively correlated with UBIAD1 expression in all tumors and
450 astrocytoma, whereas FDPS expression correlated significantly with histological grade (P = 0.008)
451 and autophagosome accumulation (P = 0.027).

452 Collectively, these data demonstrate a progressive remodeling of autophagy and cholesterol
453 metabolism pathways during glioma progression, characterized by enhanced autophagosome
454 accumulation and FDPS upregulation from astrocytoma to glioblastoma. This coordinated
455 autophagy–metabolism dysregulation defines a shared adaptive program associated with
456 malignant progression and suggests that these pathways may also contribute to therapeutic failure
457 in high-grade gliomas[46-50].

458 Given that chemoresistance remains a major clinical challenge in glioblastoma and is increasingly
459 linked to cellular stress–adaptive programs and metabolic plasticity, we next investigated whether
460 dysregulated autophagy and cholesterol metabolism are associated with resistance to TMZ. To this
461 end, we established mKate-labeled U251 TMZ-resistant (R) cells and systematically compared
462 their autophagy status and cholesterol metabolic profiles with those of TMZ-sensitive (NR)

counterparts. We further examined whether targeting cholesterol metabolism could modulate lipid homeostasis and attenuate TMZ resistance.

Notably, TMZ resistance was accompanied by phenotypic and metabolic reprogramming, including epithelial-to-mesenchymal transition (EMT), mitotic quiescence, and a broader metabolic switch, which we investigate in detail in the subsequent sections.

Table 1. Correlation of cytosolic LC3, P62, FDPS, and UBIAD protein expression and autophagic flux with clinicopathological features of Brain tumor

Parameter	Brain tissues		Age (years)		Gender		WHO grade			
	Malignant (All subtypes)	**Normal**	**≤42**	**>42**	**Male**	**Female**	**I**	**II**	**III**	**IV**
Cytosolic LC3 (N)	(68)	(10)	(34)	(34)	(38)	(30)	(12)	(24)	(8)	(24)
%None	1.5	0	2.9	0	0	3.3	8.3	0	0	0
%Weak	5.9	50	0	11.8	5.3	6.7	25	4.2	0	0
%Moderate	0	10	0	0	0	0	0	0	0	0
%Strong	92.6	40	97.1	88.2	94.7	90	66.7	95.8	100	100
p-value	**<0.0001**		0.114		0.619			**0.014**		
Cytosolic P62 (N)										
%None	(67)	(10)	(34)	(33)	(37)	(30)	(12)	(24)	(8)	(23)
%Weak	58.2	50	50	66.7	54.1	63.3	50	66.6	87.5	43.5
%Moderate	22.4	30	29.4	15.2	21.6	23.3	33.3	12.5	0	34.8
%Strong	9	20	11.8	6	13.5	3.4	0	16.7	12.5	4.3
	10.4	0	8.8	12.1	10.8	10	16.7	4.2	0	17.4
p-value	0.499		0.397		0.581			0.105		
Cytosolic FDPS (N)										
%None	(68)	(10)	(34)	(34)	(38)	(30)	(12)	(24)	(8)	(24)
%Weak	25	70	29.4	20.6	23.7	26.7	41.7	12.5	62.5	16.7
%Moderate	26.5	0	17.7	35.3	28.9	23.3	41.7	33.4	25	12.5
%Strong	22	30	23.5	20.6	21.1	23.3	8.3	33.3	12.5	20.8
	26.5	0	29.4	23.5	26.3	26.7	8.3	20.8	0	50
p-value	**0.007**		0.420[a]		0.960[a]			**0.008**		
Cytosolic UBIAD (N)										
%None	(68)	(10)	(34)	(34)	(38)	(30)	(12)	(24)	(8)	(24)
%Weak	14.7	0	17.6	11.8	21.1	6.7	25	12.5	25	8.3
%Moderate	19.1	40	23.5	14.7	21	16.7	8.3	20.8	25	20.8
%Strong	22.1	10	11.8	32.4	10.5	36.6	16.7	12.5	12.5	37.5
	44.1	50	47.1	41.1	47.4	40	50	54.2	37.5	33.4
p-value	0.344		0.213[a]		**0.048[a]**			0.493		
Autophagic flux (N)	(67)	(10)	(34)	(33)	(37)	(30)	(12)	(24)	(8)	(23)
%Very active flux	7.5	60	2.9	12.1	5.4	10	33.3	4.2	0	0
%Moderate inhibited	9	20	11.8	6.1	13.5	3.3				4.3

%Inhibited	10.4	0	8.8	12.1	10.8	10	0	16.7	12.5	17.4
%Very active autophagosome formation	73.1	20	76.5	69.7	70.3	76.7	16.7 50	4.175	0 87.5	78.3
p-value	**<0.0001**		0.453		0.503		**0.027**			

Statistical significance was tested using Fisher's exact test, except ([a]), where it was performed using Pearson's χ^2 test. *P*-value < 0.05 was considered statistically significant and highlighted in bold.

Table 2. Correlation of cytosolic LC3, P62, FDPS, and UBIAD protein expression and autophagic flux with clinicopathological features of astrocytoma

Parameter	**Brain tissues**		**Age (years)**		**Gender**		**WHO grade**			
	Astrocytoma	**Normal**	**≤39**	**>39**	**Male**	**Female**	**I**	**II**	**III**	**IV**
Cytosolic LC3 (N)	(46)	(10)	(26)	(20)	(28)	(18)	(12)	(24)	(8)	(2)
%None	2.2	0	3.8	0	0	5.6	8.3	0	0	0
%Weak	8.7	50	0	20	7.1	11.1	25	4.2	0	0
%Moderate	0	10	0	0	0	0	0	0	0	0
%Strong	89.1	40	96.2	80	92.9	83.3	66.7	95.8	100	100
p-value	**0.002**		**0.030**		0.419		0.134			
Cytosolic P62 (N)										
%None	(46)	(10)	(26)	(20)	(28)	(18)	(12)	(24)	(8)	(2)
%Weak	63	50	53.8	75	64.3	61	50	66.7	87.5	0
%Moderate	17.5	30	23.2	10	10.7	27.8	33.3	12.5	0	50
%Strong	13	20	11.5	15	17.9	5.6	0	16.7	12.5	50
	6.5	0	11.5	0	7.1	5.6	16.7	4.1	0	0
p-value	0.644		0.279		0.409		0.078			
Cytosolic FDPS (N)										
%None	(46)	(10)	(26)	(20)	(28)	(18)	(12)	(24)	(8)	(2)
%Weak	28.3	70	34.6	20	32.1	22.2	41.7	12.5	62.5	0
%Moderate	32.6	0	11.5	60	32.1	33.3	41.7	33.4	25	0
%Strong	21.7	30	23.1	20	17.9	27.8	8.3	33.3	12.50	0
	17.4	0	30.8	0	17.9	16.7	8.3	20.8		100
p-value	**0.019**		**0.001**		0.815		**0.032**			
Cytosolic UBIAD (N)										
%None	(46)	(10)	(26)	(20)	(28)	(18)	(12)	(24)	(8)	(2)
%Weak	17.4	0	11.5	25	21.4	11.1	25	12.5	25	0
%Moderate	17.4	40	15.4	20	17.9	16.7	8.3	20.8	25	0
%Strong	13	10	11.6	15	7.1	22.2	16.7	12.5	12.5	0
	52.2	50	61.5	40	53.6	50	50	54.2	37.5	100
p-value	0.344		0.446		0.524		0.939			
Autophagic flux (N)	(46)	(10)	(26)	(20)	(28)	(18)	(12)	(24)	(8)	(2)
%Very active flux	10.9	60	3.9	20	7.1	16.7		4.2	0	0

%Moderate inhibited	13	20	11.5	15	17.9	5.6	33.3	16.7	12.5	50
%Inhibited	6.5	0	11.5	0	7.1	5.6	0	4.175	0	0
%Very active autophagosome formation	69.6	20	73.1	65	67.9	72.1	16.7 50		87.5	50
p-value	**0.002**		0.188		0.563			0.077		

Statistical significance was tested using Fisher's exact test.
P-value < 0.05 was considered statistically significant and highlighted in bold.

Table 3. Correlation of cytosolic LC3, P62, FDPS, and UBIAD protein expression and autophagic flux with clinicopathological features of glioblastoma

Parameter	**Brain tissues**		**Age (years)**		**Gender**		**WHO grade**			
	Glioblastoma	**Normal**	**≤49**	**>49**	**Male**	**Female**	**I**	**II**	**III**	**IV**
Cytosolic LC3 (N)	(22)	(10)	(12)	(10)	(10)	(12)	(0)	(0)	(0)	(22)
%None	0	0	0	0	0	0	0	0	0	0
%Weak	0	50	0	0	0	0	0	0	0	0
%Moderate	0	10	0	0	0	0	0	0	0	0
%Strong	100	40	100	100	100	100	0	0	0	100
p-value	**<0.0001**		NA		NA			NA		
Cytosolic P62 (N)										(21)
%None	(21)	(10)	(12)	(9)	(9)	(12)	(0)	(0)	(0)	47.6
%Weak	47.6	50	50	44.4	22.2	66.7	0	0	0	33.1
%Moderate	33.4	30	33.3	33.3	55.6	16.7	0	0	0	0
%Strong	0	20	0	0	0	0	0	0	0	19
	19	0	16.7	22.3	22.2	16.6	0	0	0	
p-value	0.128		1.000		0.094			NA		
Cytosolic FDPS (N)										(22)
%None										18.2
%Weak	(22)	(10)	(12)	(10)	(10)	(12)	(0)	(0)	(0)	13.6
%Moderate	18.2	70	0	40	0	33.3	0	0	0	22.7
%Strong	13.6	0	25	0	20	8.3	0	0	0	45.5
	22.7	30	25	20	30	16.7	0	0	0	
	45.5	0	50	40	50	41.7	0	0	0	
p-value	**0.005**		0.059		0.264			NA		
Cytosolic UBIAD (N)										(22)
%None	(22)	(10)	(12)	(10)	(10)	(12)	(0)	(0)	(0)	9.1
%Weak	9.1	0	16.7	0	20	0	0	0	0	22.7
%Moderate	22.7	40	25	20	30	16.7	0	0	0	40.9
%Strong	40.9	10	41.6	40	20	58.3	0	0	0	27.3
	27.3	50	16.7	40	30	25	0	0	0	
p-value	0.213		0.597		0.177			NA		
Autophagic flux (N)	(21)	(10)	(12)	(9)	(9)	(12)	(0)	(0)	(0)	(21)
%Very active flux	0	60	0	0	0	0	0	0	0	0
%Moderate inhibited	0	20	0	0	0	0	0	0	0	0
%Inhibited	19	0	16.7	22.2	22.2	16.7	0	0	0	19

%Very active autophagosome formation	81	20	83.3	77.8	77.8	83.3	0	0	0	81
p-value	**<0.0001**		1.000		1.000		NA			

Statistical significance was tested using Fisher's exact test.
P-value < 0.05 was considered statistically significant and highlighted in bold.

TMZ Resistance Is Coupled to EMT, Mitotic Quiescence, and Mitochondrial Remodeling

R cells exhibited significantly reduced sensitivity to TMZ-induced cell death at concentrations ≥10 μM, consistent with our previous observations [12]. To determine whether resistance acquisition was accompanied by phenotypic reprogramming, we examined cellular morphology by bright-field microscopy. Compared with NR cells, R cells displayed an elongated, spindle-like morphology (**Figure 2A**) and a marked increase in cytoplasmic vesicular structures (**Figure 2B**), features consistent with epithelial-to-mesenchymal transition (EMT). Immunoblotting confirmed increased expression of the mesenchymal markers N-cadherin and vimentin in R cells (**Figure 2C**).

Given the reported links between autophagy and EMT, we next assessed whether acute inhibition of autophagic flux influences mesenchymal marker expression. Treatment with bafilomycin A1 (5 nM, 72 h) did not alter N-cadherin or vimentin levels in either NR or R cells (**Figure 2C**), indicating that maintenance of the mesenchymal phenotype in R cells is not dependent on short-term autophagy flux inhibition.

We then evaluated proliferative dynamics and cell-cycle status. R cells exhibited a substantially reduced proliferation rate, with total cell numbers decreasing to less than half of NR cells after 72 h **(Figure 2D**). Cell-cycle analysis revealed a greater than two-fold reduction in mitotic cells and a three-fold increase in G1-phase arrest in R cells, accompanied by a marked reduction in sub-G0/G1 apoptotic populations (**Figure 2E**), consistent with mitotic quiescence.

Because therapy resistance is frequently associated with mitochondrial adaptation, we examined mitochondrial structure and function. Transmission electron microscopy revealed pronounced mitochondrial abnormalities in R cells, including disrupted cristae architecture and increased mitophagic structures (**Figure 2F**). Live-cell mitochondrial imaging using MitoView Green showed elongated mitochondrial networks in NR cells, whereas R cells exhibited fragmented and clustered mitochondria, consistent with enhanced mitochondrial remodeling (**Figure 2G**).

To further define metabolic adaptations associated with temozolomide resistance, we assessed mitochondrial respiration in NR and R U251 glioblastoma cells using Seahorse extracellular flux analysis (**Figure 2H-I**). Basal oxygen consumption rates were comparable between NR and R cells; however, following sequential metabolic perturbations, R cells displayed a markedly blunted respiratory response compared with NR cells.

Specifically, NR cells demonstrated a robust increase in respiration following mitochondrial uncoupling, reflecting substantial spare respiratory capacity. In contrast, R cells showed a significantly attenuated response, indicating limited metabolic flexibility under stress conditions

518 (**Figure 2H**). Quantitative analysis confirmed a significant reduction in maximal respiratory
519 capacity and ATP-linked respiration in R cells relative to NR cells, consistent with an altered
520 energetic state (**Figure I**).

521 Notably, R cells exhibited increased proton leak compared with NR cells (Figure I), suggesting
522 mitochondrial inefficiency and adaptive remodeling of energy utilization rather than enhanced
523 energy production. Together, these findings indicate that acquisition of TMZ resistance is
524 accompanied by a metabolic switch characterized by constrained respiratory reserve and altered
525 mitochondrial stress handling, consistent with a low-proliferative, therapy-tolerant phenotype.

526 Collectively, these data show that acquisition of TMZ resistance is associated with coordinated
527 phenotypic and bioenergetic reprogramming, characterized by EMT, mitotic quiescence, and
528 mitochondrial remodeling, supporting the existence of a broader metabolic switch that facilitates
529 survival under chemotherapeutic stress.

530 **Cholesterol Biosynthesis Is Suppressed in TMZ-Resistant Cells in the Context of Impaired**
531 **Autophagy Flux**

532 Autophagy plays a central role in cellular lipid homeostasis by regulating membrane turnover,
533 lipid droplet utilization, and cholesterol trafficking through autophagosome–lysosome degradation
534 [51]. Impairment of autophagic flux is therefore expected to disrupt cholesterol availability and
535 biosynthetic feedback regulation. Given our previous demonstration that autophagy flux is
536 inhibited in R cells [12], together with the accumulation of autophagosomes and vesicular
537 structures observed in resistant cells, we hypothesized that TMZ resistance is associated with
538 altered cholesterol metabolism as a consequence of defective autophagy-mediated lipid recycling.

539 Consistent with this hypothesis and our previous findings, ultrastructural analysis by transmission
540 electron microscopy revealed a pronounced increase in intracellular vesicular compartments in R
541 cells, including a higher number of double-membrane vesicles characteristic of autophagosomes,
542 compared with NR cells (**Figure 3A,B**). These findings extend our earlier observations of impaired
543 autophagic clearance and support the presence of disrupted membrane and lipid turnover in
544 resistant cells.

545 Recent multi-omics analyses comparing primary and recurrent glioblastoma specimens have
546 independently identified cholesterol biosynthesis as a pathway significantly altered in TMZ-
547 resistant tumors [52]. Guided by this evidence and our autophagy findings, we quantified total de
548 novo cholesterol synthesis and cholesterol esterification in R and NR cells. Both processes were
549 significantly reduced in R cells across all examined time points (**Figure 3C,D**), indicating
550 suppression of cholesterol biosynthetic capacity in the resistant state.

551 To determine whether reduced cholesterol synthesis reflected transcriptional reprogramming, we
552 assessed the expression of LDL receptor (LDL-R), which mediates cholesterol uptake, and sterol
553 regulatory element–binding protein 2 (SREBP2), a master regulator of cholesterol biosynthesis.
554 Real-time PCR analysis revealed significantly decreased LDL-R and SREBP2 mRNA levels in R
555 cells compared with NR cells (**Figure 3E,F**), consistent with impaired cholesterol homeostasis
556 and reduced sterol-driven feedback signaling.

557 Because impaired autophagy flux may limit endogenous cholesterol recycling, we next tested
558 whether exogenous cholesterol delivery could influence cell viability or TMZ sensitivity.
559 Treatment with lipid nanoparticles (LNPs), which contain approximately 45% cholesterol by mass,
560 induced lipotoxicity in both NR and R cells (**Figure 3G**). However, LNP treatment did not
561 significantly enhance TMZ-induced cytotoxicity in R cells (**Figure 3H**), indicating that cholesterol
562 supplementation alone is insufficient to reverse established TMZ resistance.

563 Collectively, these data demonstrate that impaired autophagy flux in TMZ-resistant cells is
564 accompanied by suppression of cholesterol biosynthesis and esterification, together with
565 transcriptional downregulation of cholesterol regulatory pathways. This coordinated dysregulation
566 links defective autophagy-mediated lipid recycling to altered cholesterol metabolism and supports
567 a model in which metabolic adaptation contributes to the maintenance of TMZ resistance.

568 **Simvastatin Fails to Resensitize TMZ-Resistant Cells to TMZ-Induced Apoptosis**

569 Our previous work demonstrated that simvastatin (Simva) sensitizes glioblastoma cells to
570 temozolomide (TMZ)-induced apoptosis through inhibition of autophagic flux [36]. Given our
571 current findings that TMZ-resistant (R) cells exhibit impaired autophagy flux, suppressed
572 cholesterol biosynthesis, and extensive metabolic reprogramming, we next asked whether Simva
573 could overcome TMZ resistance in this context.

574 R cells were treated with Simva alone or in combination with TMZ, and apoptotic responses were
575 assessed. In contrast to TMZ-non-resistant (NR) cells, neither Simva monotherapy nor combined
576 Simva–TMZ treatment induced a significant increase in apoptotic cell death in R cells (**Figure**
577 **4A**). Consistently, caspase-3/7 activity (**Figure 4B**) and caspase-9 activation (**Figure 4C**) were
578 not significantly elevated in R cells following either treatment compared with NR cells.

579 These results indicate that, unlike in TMZ-sensitive cells, inhibition of the mevalonate pathway by
580 Simva is insufficient to restore TMZ-induced apoptotic signaling in the resistant state. Together
581 with our earlier data, these findings suggest that the autophagy–cholesterol axis in R cells is
582 rewired in a manner that uncouples statin-mediated autophagy modulation from apoptotic
583 execution, highlighting the robustness of the resistant phenotype.

584 **Simvastatin Exposure Reveals Cholesterol Metabolic Plasticity in TMZ-Resistant**
585 **Glioblastoma**

586 Our preceding analyses demonstrated that R glioblastoma cells exhibit impaired autophagy flux,
587 accumulation of autophagosomes, and suppression of endogenous cholesterol biosynthesis,
588 together with resistance to statin-mediated apoptotic sensitization. Because cholesterol
589 homeostasis is tightly regulated by both de novo synthesis and autophagy-dependent lipid
590 recycling, these findings raised the possibility that pharmacologic inhibition of the mevalonate
591 pathway may differentially impact cholesterol handling in resistant versus non-resistant cells.

592 Simvastatin (ST), a clinically approved HMG-CoA reductase inhibitor, directly targets the rate-
593 limiting step of cholesterol biosynthesis and has been shown to modulate autophagy and membrane
594 lipid composition in cancer cells [53, 54]. On the other hand, Acquired resistance in glioblastoma

595 is a significant hurdle in effective treatment, often associated with metabolic reprogramming,
596 including changes in cholesterol metabolism [12, 55, 56]. We therefore used ST as a metabolic
597 probe to interrogate how TMZ resistance alters cholesterol metabolic flexibility and compensatory
598 lipid remodeling. By comparing the effects of ST, TMZ, and combined TMZ–ST treatment on
599 cholesterol profiles in NR and R U251 cells, we aimed to define resistance-specific adaptations in
600 cholesterol metabolism that persist despite pharmacologic pathway inhibition. To this end, we
601 performed comprehensive lipidomic analyses of free cholesterol and cholesterol esters to assess
602 how R and NR cells differentially remodel cholesterol pools in response to ST-based perturbation.

603 A comprehensive heatmap analysis revealed significant alterations in cholesterol profiles,
604 including free cholesterol and a range of cholesterol esters (CE 14:0 to CE 22:6), between NR
605 and R glioblastoma cells under various treatment conditions (**Figure 5A**). Principal Component
606 Analysis (PCA) further demonstrated distinct clustering of NR and R cells treated with
607 Simvastatin (ST), TMZ, and combined TMZ-ST, underscoring the metabolic reprogramming
608 associated with resistance and differential treatment responses (**Figure 5B**). Volcano plot
609 analysis revealed that, in control groups, CE 22:0 levels were significantly increased in R cells
610 compared to NR cells, indicating inherent differences in cholesterol metabolism associated with
611 resistance (**Figure 5G**). Under ST treatment, several cholesterol esters, including CE 22:6, CE
612 22:4, and CE 22:5, were significantly upregulated in R cells, with amplified changes observed in
613 R cells, indicating a resistance-mediated adaptation to ST treatment (**Figure 5H**). Interestingly,
614 TMZ treatment alone did not result in significant changes in cholesterol esters, suggesting limited
615 effects of TMZ on cholesterol metabolism (**Figure 5I**). However, combined TMZ-ST treatment
616 led to a significant upregulation in multiple cholesterol esters, including CE 22:5, CE 22:4, and
617 CE 22:6, with the most pronounced effects observed in R cells, highlighting the synergistic
618 potential of this combination (**Figure 5J**). Quantitative analyses of cholesterol components,
619 including free cholesterol and specific esters (CE 16, CE 17, CE 18, CE 20, and CE 22),
620 confirmed these trends, with R cells consistently exhibiting higher levels compared to NR cells
621 across all treatment groups (except CE 18:1), particularly under combined TMZ-ST therapy
622 (**Figure 5K-Q**). Our findings reveal that TMZ resistance in GB cells is associated with significant
623 alterations in cholesterol metabolism. While ST and the ST-TMZ combination disrupted CE
624 profiles, neither treatment induced apoptosis or activated Caspase-3/-7 or Caspase-9 in R cells
625 compared to NR cells. Our KEGG analysis (**Figure 5R snd D**) revealed that the top five pathways
626 associated with differences between R and NR GB cells were Steroid hormone biosynthesis,
627 Ovarian steroidogenesis, Neuroactive ligand-receptor interaction, Insulin resistance, and
628 Metabolic pathways. These pathways are intricately linked to autophagy, providing a strong
629 rationale for its investigation in validating our lipidomics results. Steroid hormone biosynthesis
630 influences autophagy through glucocorticoids, which modulate autophagic flux by interacting
631 with key pathways such as mTOR [57]. Similarly, Ovarian steroidogenesis involves estrogen and
632 progesterone, which regulate autophagy in various cellular contexts, including cancer [58, 59].
633 The Neuroactive ligand-receptor interaction pathway highlights neurotransmitters and receptors
634 that impact autophagy via calcium signaling and neurotrophic factors [60]. Insulin resistance
635 directly alters autophagy by disrupting glucose metabolism and activating stress responses critical

636 for cellular adaptation [61]. Lastly, Metabolic pathways broadly integrate lipid and energy
637 metabolism with autophagic processes to regulate lipid turnover and maintain homeostasis [62].
638 These findings underscore the significant role of autophagy in these pathways, justifying its
639 investigation in the next section as a biological validation of our lipidomics findings.

640 **Simvastatin and Temozolomide Fail to Restore Autophagy Flux in TMZ-Resistant**
641 **Glioblastoma Cells**

642 To functionally validate our lipidomic findings and determine whether pharmacologic
643 perturbation of cholesterol metabolism influences autophagy in the resistant state, we examined
644 the effects of temozolomide (TMZ; 100 μM), simvastatin (Simva; 1 μM), and combined TMZ–
645 Simva treatment on autophagy flux in U251 NR and R glioblastoma cells over 72 hours.
646 Autophagy flux was assessed using transmission electron microscopy (TEM) and immunoblot
647 analysis of LC3β and p62/SQSTM1 (**Figure 6A,B**).

648 TEM analysis revealed no significant changes in the number or morphology of double-membrane
649 autophagosomes in R cells across all treatment conditions, indicating persistent autophagosome
650 accumulation irrespective of TMZ, Simva, or combination treatment (**Figure 6A**). In contrast,
651 NR cells displayed a clear increase in autophagosome number following TMZ, Simva, or TMZ–
652 Simva exposure, consistent with treatment-induced perturbation of autophagy dynamics.

653 Immunoblot analysis corroborated these ultrastructural findings. In NR cells, Simva and TMZ–
654 Simva treatment resulted in accumulation of LC3β-II and impaired degradation of p62, indicative
655 of autophagy flux inhibition (**Figure 6B**). By contrast, LC3β-II levels and p62 abundance
656 remained unchanged in R cells following all treatments, consistent with an already established
657 blockade of autophagy flux that is refractory to further pharmacologic modulation.

658 Together, these data demonstrate that neither TMZ nor simvastatin, alone or in combination, is
659 sufficient to restore autophagy flux or alter autophagosome turnover in TMZ-resistant
660 glioblastoma cells. This fixed autophagy-blocked state likely contributes to the stability of the
661 resistant phenotype and underscores the challenge of targeting autophagy as a therapeutic
662 vulnerability in established TMZ resistance.

663

664 **Discussion**

665 Our findings reveal distinct autophagy marker patterns (LC3β and p62) in brain tumors and
666 adjacent normal tissues, highlighting differences in autophagic activity. Tumor tissues exhibit
667 increased autophagosome formation but impaired autophagic flux, leading to vesicle accumulation
668 rather than degradation. In contrast, normal tissues show higher autophagy flux, maintaining
669 metabolic balance. This dysregulated autophagy in tumors may sustain metabolic intermediates
670 and enhance tumor survival under stress [63].

671 Autophagy and cholesterol biosynthesis play key roles in astrocytoma and GB pathogenesis. A
672 strong correlation between LC3β puncta and autophagy activity suggests increased

673 autophagosome formation as an adaptive mechanism to sustain energy and manage tumor
674 metabolic stress [64, 65]. A positive correlation between LC3β puncta and UBIAD expression
675 suggests autophagy supports cholesterol biosynthesis for tumor survival. Meanwhile, p62
676 accumulation inversely correlates with autophagy flux, indicating impaired autophagic
677 degradation. In GB, UBIAD downregulation further links autophagy dysfunction to cholesterol
678 metabolism dysregulation [66-68]. An important aspect highlighted by our tissue-based analyses
679 is that dysregulation of autophagy and cholesterol metabolism is not a binary feature of
680 glioblastoma but instead emerges progressively during glioma evolution from astrocytoma to
681 glioblastoma. Astrocytomas already display elevated autophagosome accumulation and increased
682 FDPS expression compared with normal brain tissue, indicating that autophagy–lipid coupling is
683 engaged early in tumorigenesis. However, this state remains heterogeneous, with partial
684 preservation of autophagic flux and metabolic flexibility. In contrast, glioblastomas exhibit a
685 uniform phenotype characterized by robust autophagosome accumulation, near-complete loss of
686 effective autophagic flux, and pronounced upregulation of FDPS, reflecting a fully established
687 autophagy–cholesterol rewiring program. This stepwise intensification suggests that progressive
688 uncoupling of autophagosome formation from degradation, together with reinforcement of
689 cholesterol biosynthetic and buffering pathways, contributes to malignant progression and
690 metabolic hardening. Thus, autophagy flux blockade and cholesterol pathway remodeling appear
691 to function as adaptive layers that accumulate with tumor grade, predisposing high-grade gliomas
692 to stress tolerance and therapeutic resistance. Thus, autophagy flux blockade and cholesterol
693 pathway remodeling appear to function as adaptive layers that accumulate with tumor grade,
694 predisposing high-grade gliomas to stress tolerance and therapeutic resistance in part through
695 metabolic reprogramming and lipid homeostasis alterations [23, 69, 70].

696 TMZ-resistant GB cells undergo EMT, mitotic quiescence, and a metabolic shift to OXPHOS,
697 enhancing survival. Resistant cells exhibit elongated morphology, increased vesicles, and
698 upregulated EMT markers (N-cadherin, Vimentin), promoting invasiveness, plasticity, and
699 therapy resistance [71, 72]. Blocking autophagy flux with Bafilomycin A1 did not affect EMT
700 marker expression, suggesting EMT persists independently of autophagy. Resistant cells exhibit
701 mitotic quiescence, marked by reduced proliferation, fewer mitotic cells, and G1 phase arrest,
702 mirroring stem-like traits that enhance survival under chemotherapy [73]. Mitotic quiescence
703 shields cells from TMZ-induced apoptosis, as reflected by a lower sub-G0-G1 population, and
704 allows them to conserve energy and evade cellular stress associated with rapid proliferation [74].
705 This quiescent state, often linked to tumor-initiating cells, could serve as a reservoir for recurrence
706 post-treatment, highlighting a critical therapeutic challenge in GB management [75].

707 The metabolic phenotype associated with temozolomide resistance in glioblastoma appears to
708 reflect an adaptive state geared toward stress tolerance rather than enhanced bioenergetic output.
709 Rather than increasing mitochondrial ATP production or respiratory reserve, resistant cells adopt
710 a constrained energetic program characterized by reduced metabolic flexibility. This shift is
711 consistent with a broader therapy-tolerant phenotype in which survival is favored over
712 proliferation, aligning with the observed mitotic quiescence and reduced growth capacity of
713 resistant cells. Elevated proton leak in resistant cells suggests adaptive mitochondrial uncoupling,
714 a mechanism that may limit oxidative stress and preserve cellular integrity under chronic
715 therapeutic pressure [76, 77]. Such uncoupling has been proposed as a survival strategy in cancer
716 cells exposed to sustained stress, allowing maintenance of redox balance and mitochondrial

717 function without committing to high-energy-demand states [77]. In this context, mitochondrial
718 remodeling reflects functional adaptation rather than optimization of oxidative metabolism.

719 Additionally, our findings corroborate previous evidence [3], indicating that TMZ resistance is
720 associated with inhibited autophagy flux. Autophagy can promote both survival and cell death, but
721 in resistant cells, blocking autophagy flux allows vesicle accumulation, buffering metabolic stress
722 and sustaining homeostasis. This aligns with studies showing autophagy flux inhibition as a
723 strategy for cancer cells to evade apoptosis and adapt to chemotherapy [78].

724 In TMZ-resistant cells, we observed a blockade of autophagy flux, as indicated by autophagosome
725 accumulation, disrupting lipophagy, the process responsible for degrading lipid droplets and
726 recycling cholesterol. Cholesterol plays a critical role in regulating autophagy, particularly in the
727 formation and maturation of autophagosomes. Cholesterol is an essential component of cellular
728 membranes, including the membranes of autophagosomes and lysosomes, which are crucial for
729 maintaining autophagy flux[62, 68, 79]. This impaired autophagic clearance reduces cholesterol
730 availability, reflected by decreased de novo cholesterol synthesis and the downregulation of
731 cholesterol biosynthesis genes, such as SREBP-2 and LDL-R. To compensate, R cells reprogram
732 their lipid metabolism, shifting towards cholesterol esterification, as evidenced by the increase in
733 specific cholesterol esters (CEs), including CE 22:5, CE 22:6, and CE 20:4. This metabolic shift
734 allows R cells to store cholesterol in a non-toxic form, buffering against oxidative and metabolic
735 stress while creating a reservoir of lipids that may support membrane synthesis and structural
736 integrity under stress[16, 23, 80]. Despite clear evidence that temozolomide-resistant cells exhibit
737 suppressed de novo cholesterol biosynthesis and transcriptional downregulation of LDL-R and
738 SREBP-2, exogenous cholesterol delivery via lipid nanoparticles (LNPs) failed to restore
739 chemosensitivity or reverse resistance. This finding suggests that cholesterol limitation per se is
740 not the dominant vulnerability in resistant cells. Instead, resistant glioblastoma cells appear
741 metabolically entrenched in a state that favors cholesterol sequestration and esterification rather
742 than utilization for membrane synthesis or signaling. The observed lipotoxicity induced by LNPs
743 in both resistant and non-resistant cells further supports the notion that excess free cholesterol
744 cannot be productively integrated into cellular metabolism when autophagic lipid recycling is
745 impaired. In resistant cells, autophagy flux blockade likely prevents efficient redistribution and
746 turnover of exogenous lipids, rendering cholesterol supplementation ineffective as a
747 resensitization strategy. These results emphasize that metabolic dependencies in chemoresistant
748 glioblastoma are shaped not only by substrate availability but also by intracellular trafficking and
749 degradation capacity. Therapeutic strategies aimed at overcoming resistance will therefore need to
750 disrupt both lipid storage pathways and the autophagy machinery that buffers metabolic stress,
751 rather than attempting to replenish depleted metabolites alone [23, 81, 82].

752 The ST and TMZ-ST treatments further highlight metabolic reprogramming. While TMZ alone
753 induces minimal changes in CEs, the combined TMZ-ST treatment amplifies CE alterations,
754 suggesting that targeting cholesterol metabolism can exacerbate stress in resistant cells [83-85].
755 GB relies on cholesterol esterification, driven by the increased activity of Sterol O-acyltransferase
756 1 (SOAT1), also known as acyl-CoA:cholesterol acyltransferase 1 (ACAT1), which converts free
757 cholesterol into cholesteryl esters stored in lipid droplets. SOAT1 is overexpressed in GB,

758 promoting lipid accumulation, tumor progression, and poor patient survival. Inhibiting SOAT1
759 reduces cholesterol esterification, leading to free cholesterol buildup in the endoplasmic reticulum
760 (ER). This disrupts lipid metabolism by suppressing sterol regulatory element-binding protein-1
761 (SREBP-1), reducing fatty acid synthesis and impairing tumor growth. Preclinical studies show
762 that genetic silencing of SOAT1 and pharmacological inhibition (e.g., avasimibe and K604)
763 significantly decrease GB cell viability and tumor progression [23, 86-89]. Impaired autophagy
764 flux further exacerbates this dependency by limiting the clearance of lipid droplets and organelles,
765 reinforcing the need for alternative lipid storage mechanisms. This interplay between autophagy
766 and lipid metabolism represents a dual vulnerability in R cells. The blockade of autophagy flux
767 increases dependency on CE accumulation and disrupts cellular homeostasis, forcing metabolic
768 adaptations to sustain chemoresistance. The accumulation of cholesteryl esters and triglycerides
769 in high-grade tumor extracts is associated with the extent of vascular proliferation, distinguishing
770 them from both normal brain tissue and low-grade neoplasms[90].

771 Our findings reveal a compelling connection between autophagy dysregulation and metabolic
772 reprogramming in R GB cells, providing key insights into mechanisms of chemoresistance. KEGG
773 pathway enrichment identified Steroid hormone biosynthesis, Ovarian steroidogenesis,
774 Neuroactive ligand-receptor interaction, Insulin resistance, and Metabolic pathways as the top
775 pathways differentiating R and TMZ-sensitive (NR) cells. These pathways are intricately linked
776 to autophagy, underscoring its central role in regulating cellular adaptation. Steroid hormones,
777 including glucocorticoids, are known to modulate autophagy through signaling pathways that
778 converge on mTOR-dependent and stress-responsive regulatory networks, with mTOR acting as a
779 central integrator of hormonal and metabolic cues controlling autophagic activity [91, 92].
780 Similarly, steroid hormones associated with ovarian steroidogenesis, including estrogen and
781 progesterone, have been reported to modulate autophagy in specific cancer contexts [93-95]. The
782 Neuroactive ligand-receptor interaction pathway highlights the role of neurotransmitters and
783 calcium signaling in regulating autophagy [96, 97], while Insulin resistance disrupts glucose
784 metabolism and activates stress responses that directly alter autophagic flux [98]. Finally,
785 Metabolic pathways integrate lipid and energy metabolism with autophagic processes,
786 coordinating lipid turnover and homeostasis [29, 99, 100].

787 This study demonstrates that glioblastoma progression and temozolomide resistance are
788 underpinned by a coordinated interconnection of autophagy and lipid metabolism rather than by
789 isolated pathway alterations. Brain tumors exhibit a characteristic pattern of increased
790 autophagosome formation coupled with impaired autophagic flux, distinguishing malignant tissue
791 from adjacent normal brain and establishing vesicle accumulation as a hallmark of tumor-
792 associated metabolic stress adaptation. In glioblastoma, this dysregulated autophagy state is tightly
793 linked to alterations in cholesterol handling, including suppressed de novo cholesterol synthesis,
794 transcriptional downregulation of SREBP-2 and LDL-R, and compensatory cholesterol ester
795 accumulation.

796 In the context of temozolomide resistance, these alterations converge into a stable, therapy-tolerant
797 phenotype characterized by epithelial-to-mesenchymal transition, mitotic quiescence, constrained
798 bioenergetic capacity, and adaptive mitochondrial uncoupling. Rather than enhancing ATP

production, resistant cells adopt an energy-conserving state that limits oxidative stress and preserves cellular integrity under chronic therapeutic pressure. Importantly, pharmacologic modulation of cholesterol biosynthesis or autophagy flux alone is insufficient to restore chemosensitivity, underscoring the robustness of this adaptive program.

Together, our findings identify autophagy flux blockade and cholesterol esterification as interconnected features of glioblastoma resistance biology. This autophagy–lipid axis supports survival under treatment stress and represents a central organizing principle of chemoresistance, providing a unifying framework that links vesicle dynamics, metabolic plasticity, and therapeutic failure in glioblastoma.

These results highlight several important avenues for future investigation. First, mechanistic studies are needed to define how autophagy flux blockade is established and maintained in resistant glioblastoma cells, including the upstream regulatory events that decouple autophagosome formation from lysosomal degradation. Dissecting whether this blockade arises from lysosomal dysfunction, membrane lipid composition changes, or signaling rewiring will be critical.

Second, the reliance of resistant cells on cholesterol esterification suggests that simultaneous targeting of lipid storage pathways (e.g., SOAT1/ACAT1 inhibition) and autophagy regulation may represent a more effective strategy than single-pathway interventions. Future work should evaluate combinatorial approaches that disrupt both lipid buffering capacity and vesicle turnover to destabilize the resistant metabolic state.

Third, the metabolic adaptations observed here—mitotic quiescence, reduced respiratory reserve, and adaptive mitochondrial uncoupling—raise the possibility that resistance is sustained by stress-tolerant, low-proliferative cell populations. Longitudinal and single-cell analyses will be essential to determine whether these cells serve as reservoirs for recurrence and how they transition back to proliferative states following treatment withdrawal.

Finally, extending these findings to patient-derived models and clinical samples will be crucial to establish the translational relevance of the autophagy–cholesterol axis. Biomarkers reflecting autophagy flux status and lipid metabolic remodeling may aid in stratifying patients and guiding rational combination therapies aimed at overcoming temozolomide resistance.

Figure 1: Immunohistochemical Staining for Autophagy and Cholesterol Metabolism Proteins in Human Brain Tissues. (A) LC3 puncta Expression: LC3 puncta, an autophagosome marker, was evaluated in brain tissue using TMA. Three pathologists assessed the staining blindly, categorizing it as None, Weak, Moderate, or Strong. Results showed significantly higher LC3 puncta in astrocytoma and GB tissues compared to normal brain tissue ($P < 0.0001$). LC3 expression is linked to astrocytoma ($P < 0.01$) and GB ($P < 0.0001$) tumors. Scale bar = 50 µM. **(B) p62 Expression:** p62, a marker for autophagosome degradation, was similarly evaluated. No significant difference in p62 expression was found between normal and tumor tissues ($P = 0.499$). p62 expression is not associated with astrocytoma ($P = 0.644$) or GB ($P = 0.128$) tumors. Scale bar = 50 µM. **(C) FDPS Expression:** FDPS, a cholesterol biosynthesis pathway enzyme, in its active form, was detected in brain tissue TMA. Results indicated significant differences in FDPS expression between normal and tumor tissues ($P < 0.01$), with associations found for astrocytoma ($P < 0.5$) and GB ($P < 0.01$). Scale bar = 50 µM. **(D) UBIAD Expression:**UBIAD, a cholesterol biosynthesis pathway enzyme, also in its active form, was analyzed with no significant difference in expression between normal and tumor tissues ($P = 0.344$). UBIAD is not associated with astrocytoma ($P = 0.344$) or GB ($P = 0.213$) tumors. Scale bar = 50 µM. **(E) Correlation Analysis:** Spearman's correlation analysis examined the relationship between autophagy and MVA pathway proteins in different brain tumors. Significant correlations are marked as * ($P \leq 0.05$), *** ($P \leq 0.001$), and **** ($P \leq 0.0001$).

Figure 2. **Stem-like signature of acquired resistance**. (**A**) Bright field imaging comparing R with NR. (**B**) Western blotting of N-cadherin and Vimentin compared between NR and R without treatment and after treatment with Bafilomycin a1 5nM for 72hrs. (**C**) Proliferation assay comparing the number of the cells 72hrs after seeding 500 cell/ml. (**D**) Flow cytometer results of cell cycle assay comparing R with NR after 48hrs treatment with 250µM TMZ. (**E**) TEM images compared mitochondrial structure between NR with R. Black arrows show the mitochondria and white arrows show the mitophagosomes. (**F**) Live cell IF imaging of mitochondria using mitoviewGreen, arrow shows mitochondria. (**G**) Oxygen consumption rates (OCR) were analyzed using a Seahorse XFe24 Analyzer and normalized to cell count. Mean ATP production, and proton leak normalized to cell count were calculated. Scale bar=20 um. TEM: The transmission electron microscope. N=3 and 8 biological independent experiment in (**A-F**) and (**G-H**) respectively. ** means $P \leq 0.01$, *** means $P \leq 0.001$.

Figure 3. **Autophagy Flux Inhibition and Altered Cholesterol Biosynthesis in Acquired Resistance**. (**A & B**) TEM images compared cellular and intracellular structure between NR with R, arrows show the autophagosomes. (**C**) Total de novo synthesized cholesterol after 24, 48 and 72 hrs culture. It revealed significant decrease in total de novo synthesized cholesterol in R cells in all timepoints. (**D**) De novo Cholesterol esterification after 24, 48 and 72 hrs culture. (**E**) Real-time PCR measured the expression level of LDL-R and (**F**) SREBP-2 genes. LNP induced significant lipooxicity in both NR and R cells (**G**) while did not increase significant change in TMZ-induced cytotoxic effect in R cells (**H**). ** means $P \leq 0.01$, *** means $P \leq 0.001$.

Figure 4. **Simva and TMZ-Simva treatment do not induces apoptosis in U251 R cells**. U251 NR and R cells were treated with TMZ (100 µM), Simva (1 µ) and TMZ-Simva for 72 h. Apoptosis

869 was evaluated using propidium idodide Nicoletti assay and caspase-3/-7 and -9 luminometric
870 assay. TMZ, Simva and TMZ-Simva treatment did not induce any apoptosis (**A**), caspase-3/-7 (**B**),
871 and caspase-9 activation (**C**). All experiments were done in 3 independent biological replicates.
872 ** means $P \leq 0.01$, *** means $P \leq 0.001$.

873 **Figure 5. Impact of Temozolomide (TMZ), Simvastatin (ST), and Combined TMZ-ST**
874 **Treatment on Cholesterol Metabolism in U251 Non-Resistant NR and R Glioblastoma Cells.**
875 **A)** Heatmap generated using pheatmap illustrating the effects of Temozolomide (TMZ),
876 Simvastatin (ST), and combined TMZ-ST treatment on cholesterol metabolism in U251 Non-
877 Resistant (NR) and Resistant (R) glioblastoma cells. The heatmap includes free cholesterol and a
878 series of cholesterol esters, ranging from CE 14:0 to CE 22:6, to highlight changes in cholesterol
879 profiles under different treatment conditions (average of n=3). **B)** Principal Component Analysis
880 (PCA) of cholesterol lipids visualized using LipidSuite MetaboAnalyst 6.0 for control, ST treated,
881 TMZ treated, and combined ST-TMZ treated in U251 NR and R cells. Each treatment group
882 consists of three replicates (n=3). **C-F)** Heatmap illustrating comparison of cholesterol lipid
883 profiles in control (C), ST treatment (D), TMZ treatment (E), and combined TMZ-ST treatment
884 (F) groups in U251 NR and R cells. Each group represents the average of three replicates (n=3).
885 **G-J)** Volcano plots generated through MetaboAnalyst 6.0 illustrating differential expression of
886 cholesterol species (Free Cholesterol and Cholesterol Esters) in U251 R cells compare to U251
887 NR cells. Comparisons include control vs. treatments with Simvastatin (ST), Temozolomide
888 (TMZ), and combined TMZ-ST. Treatments are designated as follows: control (no treatment) (G),
889 ST (H), TMZ (I), and TMZ-ST (J). Each treatment has done for three replicates (n=3). In the
890 comparison between NR and R control groups, the volcano plot highlights an increase in CE 22:0
891 cholesterol ester levels in the resistant group, indicating differential cholesterol metabolism
892 associated with treatment resistance in U251 glioblastoma cells (G). In the ST treatment comparing
893 NR vs R cells, the volcano plot highlights several cholesterol esters that are significantly altered.
894 CE 22:6, CE 22:4, and CE 22:5 are the most significantly downregulated upregulated cholesterol
895 esters, suggesting their levels are substantially lower higher in resistant (R) cells compared to non-
896 resistant (NR) cells when treated with Simvastatin. CE 20:0 and CE 20:5 also show notable up
897 regulation downregulation. In contrast, CE 18:0 does not exhibit as strong a change as the others.
898 These alterations indicate a distinct lipidomic profile response to ST treatment between NR and R
899 U251 glioblastoma cells (H). Volcano plot showing the effects of Temozolomide (TMZ) treatment
900 on cholesterol ester profiles in U251 NR and R cells. The analysis reveals no meaningful changes
901 in the levels of cholesterol esters, indicating a lack of differential expression between treated and
902 control groups for the compounds analyzed (n=3) (I). Volcano plot illustrating changes in
903 cholesterol ester profiles between NR and R U251 cells following TMZ-ST treatment. The plot
904 shows an increase in the levels of CE 22:5, CE 22:4, CE 22:6, CE 22:0, CE 20:5, CE 20:3, CE
905 20:4, CE 16:2, and CE 18:2 in R cells compared to NR cells, suggesting a differential lipid
906 metabolic response to combined drug treatment (n=3) (J). **K-Q)** Concentration of cholesterol
907 family components (Free Cholesterol, CE 14, CE 16, CE 17, CE 18, CE 20, CE 22) in U251 NR
908 and R cells treated with ST, TMZ, and TMZ-ST that generated by GraphPad Prism 10. This
909 comparison highlights the differential lipid metabolic responses to the treatments across the two
910 cell lines. **R)** Subpanel R shows a protein–protein interaction (PPI) network constructed from
911 genes associated with cholesterol metabolic remodeling in R cells following TMZ, ST, and

combined TMZ–ST treatment. Nodes represent individual proteins and edges denote known or predicted interactions. Proteins highlighted in red indicate highly connected hub nodes within the network, including key enzymes involved in cholesterol and steroid metabolism (e.g., AKR1C family members, HSD17B enzymes, and cytochrome P450–related proteins). The presence of these hubs within a densely interconnected network supports coordinated metabolic and stress-adaptive signaling underlying cholesterol plasticity and drug resistance in TMZ-resistant glioblastoma cells**. S**) Subpanel S depicts pathway enrichment analysis of genes associated with cholesterol metabolism in U251 R cells following TMZ, ST, and combined TMZ–ST treatment. The top enriched pathways include Steroid hormone biosynthesis, Ovarian steroidogenesis, Neuroactive ligand–receptor interaction, Insulin resistance, and Metabolic pathways. Color intensity reflects adjusted P values, while bubble size indicates the number of genes contributing to each pathway. These enrichments support coordinated metabolic and stress-adaptive reprogramming underlying cholesterol plasticity and drug resistance.

Figure 6. **TMZ, Simva and TMZ-Simva treatment do not change autophagy flux inhibition in U251 R cells**. U251 NR and R cells were treated with TMZ (100 μM), Simva (1 μ) and TMZ-Simva for 72 h. Autophagy flux was evaluated using TEM (**A**) and immunoblotting (**B**). TEM showed no further changes in number of double membrane vacuoles in R cells in all treatments while increased them in NR cells (**A**). Immunoblotting analysis showed that Simva and Simva-TMZ treatment induced LC3β-II accumulation and inhibits p62 degradation in NR cells while it did induce any significant changes in LC3β-II accumulation and inhibits p62 degradation in R cells (**B**). All experiments were done in 3 independent biological replicates ** means $P \leq 0.01$, *** means $P \leq 0.001$.

Author Contirbution: **Shahla Shojaei** and **Amir Barzegar Behrooz** contributed to drafting the manuscript and performing experiments; **Kianoosh Naghibzadeh**, **João Basso**, **Tania Dehesh**, **Chris Pasco**, **Amir Ravandi**, **Rui Vitorino**, and **Stevan Pešić** performed lipidomics and related analyses; **Javad Alizadeh** conducted autophagy assays; **Roham Sabei** and **Bhavya Bhushan** performed experiments related to Figure 6; **Mehdi Eshraghi** contributed to manuscript drafting; **Simone De Silva Rosa**, **Courtney Clark**, **Vinith Yathindranath**, and **Donald Miller** performed and led LNP-related studies; **Mateusz Tomczyk**, **Laura Cole**, **Grant Hatch**, and **Vern Dolinsky** conducted LDL, SREBP, and cholesterol metabolism studies; **Sanjiv Dhingra** and **Abhay Srivastava** performed mitochondrial metabolism studies; **Negar Azarpira** conducted tissue pathology analysis; **Mahmoud Aghaei** performed tissue microarray and correlation analyses; **Saeid Ghavami** conceived and led the project, supervised the research, coordinated collaborations, and finalized the manuscript.

Acknowledgment: We acknowledge the use of ChatGPT (version 5.2, OpenAI) for supervised grammar editing and language refinement of the manuscript.

Funding: This work was supported by Research Manitoba New Investigator Operating Grant and University Collaborative Research Program, Dr. Carla Vitorino for insights on proteomic study. João Basso acknowledges the Portuguese Foundation for Science and Technology (FCT) for the PhD research grant (SFRH/BD/149138/2019). Simone C. da Silva Rosa is supported by CIHR postdoctoral fellowship. Bhavya Bhushan supported by CCMF and CHRIM summer

studentship. Javad Alizadeh was supported by Canada Vanier PhD studentship. Partial support was provided by the National Institute of General Medical Sciences of the National Institutes of Health under award number R16GM149204. The content is solely the responsibility of the authors and does not necessarily represent the official views of the National Institutes of Health (Stevan Pecic).

References:

1. Emir, S.M., et al., *Hunting glioblastoma recurrence: glioma stem cells as retrospective targets.* Am J Physiol Cell Physiol, 2025. **328**(3): p. C1045-c1061.
2. Pouyan, A., et al., *Glioblastoma multiforme: insights into pathogenesis, key signaling pathways, and therapeutic strategies.* Mol Cancer, 2025. **24**(1): p. 58.
3. Yan, Y., et al., *Targeting autophagy to sensitive glioma to temozolomide treatment.* J Exp Clin Cancer Res, 2016. **35**: p. 23.
4. Teraiya, M., H. Perreault, and V.C. Chen, *An overview of glioblastoma multiforme and temozolomide resistance: can LC-MS-based proteomics reveal the fundamental mechanism of temozolomide resistance?* Front Oncol, 2023. **13**: p. 1166207.
5. Wu, H., et al., *Research progress of drug resistance mechanism of temozolomide in the treatment of glioblastoma.* Heliyon, 2024. **10**(21): p. e39984.
6. Hwang, Y.K., et al., *Importance of Autophagy Regulation in Glioblastoma with Temozolomide Resistance.* Cells, 2024. **13**(16).
7. Koh, M., et al., *ANXA2 (annexin A2) is crucial to ATG7-mediated autophagy, leading to tumor aggressiveness in triple-negative breast cancer cells.* Autophagy, 2024. **20**(3): p. 659-674.
8. Wang, H., et al., *Long Non-Coding RNA NNT-AS1 Contributes to Cisplatin Resistance via miR-1236-3p/ATG7 Axis in Lung Cancer Cells.* Onco Targets Ther, 2020. **13**: p. 3641-3652.
9. Yu, W., L. Ma, and X. Li, *DANCR promotes glioma cell autophagy and proliferation via the miR-33b/DLX6/ATG7 axis.* Oncol Rep, 2023. **49**(2).
10. Qin, Y., et al., *Autophagy machinery in glioblastoma: The prospect of cell death crosstalk and drug resistance with bioinformatics analysis.* Cancer Letters, 2024. **580**: p. 216482.
11. Clark, C., et al., *Assessing Autophagy Flux in Glioblastoma Temozolomide Resistant Cells.* Methods Mol Biol, 2025. **2879**: p. 225-238.
12. Clark, C., et al., *BCL2L13 Influences Autophagy and Ceramide Metabolism without Affecting Temozolomide Resistance in Glioblastoma.* bioRxiv, 2024.
13. Meena, D. and S. Jha, *Autophagy in glioblastoma: A mechanistic perspective.* International Journal of Cancer, 2024. **155**(4): p. 605-617.
14. DeBerardinis, R.J., et al., *The biology of cancer: metabolic reprogramming fuels cell growth and proliferation.* Cell Metab, 2008. **7**(1): p. 11-20.
15. Eyme, K.M., et al., *Targeting de novo lipid synthesis induces lipotoxicity and impairs DNA damage repair in glioblastoma mouse models.* Sci Transl Med, 2023. **15**(679): p. eabq6288.
16. Weng, X., et al., *Lipidomics-driven drug discovery and delivery strategies in glioblastoma.* Biochim Biophys Acta Mol Basis Dis, 2025. **1871**(3): p. 167637.
17. Kao, T.J., et al., *Dysregulated lipid metabolism in TMZ-resistant glioblastoma: pathways, proteins, metabolites and therapeutic opportunities.* Lipids Health Dis, 2023. **22**(1): p. 114.
18. Yamamoto, Y., et al., *Intracellular cholesterol level regulates sensitivity of glioblastoma cells against temozolomide-induced cell death by modulation of caspase-8 activation via death receptor 5-accumulation and activation in the plasma membrane lipid raft.* Biochem Biophys Res Commun, 2018. **495**(1): p. 1292-1299.
19. Ahmad, F., et al., *Cholesterol Metabolism: A Potential Therapeutic Target in Glioblastoma.* Cancers (Basel), 2019. **11**(2).
20. Villa, G.R., et al., *An LXR-Cholesterol Axis Creates a Metabolic Co-Dependency for Brain Cancers.* Cancer Cell, 2016. **30**(5): p. 683-693.
21. Sato, R., *Sterol metabolism and SREBP activation.* Arch Biochem Biophys, 2010. **501**(2): p. 177-81.

1011 22. Yahagi, N., et al., *A crucial role of sterol regulatory element-binding protein-1 in the regulation of*
1012 *lipogenic gene expression by polyunsaturated fatty acids.* J Biol Chem, 1999. **274**(50): p. 35840-4.
1013 23. Guo, X., et al., *Cholesterol metabolism and its implication in glioblastoma therapy.* J Cancer, 2022.
1014 **13**(6): p. 1745-1757.
1015 24. Meyer, N., et al., *Autophagy activation, lipotoxicity and lysosomal membrane permeabilization*
1016 *synergize to promote pimozide- and loperamide-induced glioma cell death.* Autophagy, 2021.
1017 **17**(11): p. 3424-3443.
1018 25. Geng, F., et al., *SREBP-1 upregulates lipophagy to maintain cholesterol homeostasis in brain tumor*
1019 *cells.* Cell Reports, 2023. **42**(7): p. 112790.
1020 26. Kanzawa, T., et al., *Role of autophagy in temozolomide-induced cytotoxicity for malignant glioma*
1021 *cells.* Cell Death Differ, 2004. **11**(4): p. 448-57.
1022 27. Xia, Q., et al., *Therapeutic Potential of Autophagy in Glioblastoma Treatment With*
1023 *Phosphoinositide 3-Kinase/Protein Kinase B/Mammalian Target of Rapamycin Signaling Pathway*
1024 *Inhibitors.* Front Oncol, 2020. **10**: p. 572904.
1025 28. Hu, Y.L., et al., *Hypoxia-induced autophagy promotes tumor cell survival and adaptation to*
1026 *antiangiogenic treatment in glioblastoma.* Cancer Res, 2012. **72**(7): p. 1773-83.
1027 29. Xie, Y., et al., *Interplay Between Lipid Metabolism and Autophagy.* Front Cell Dev Biol, 2020. **8**: p.
1028 431.
1029 30. Zhang, S., et al., *The regulation, function, and role of lipophagy, a form of selective autophagy, in*
1030 *metabolic disorders.* Cell Death Dis, 2022. **13**(2): p. 132.
1031 31. Li, X., et al., *Crosstalk between lipid droplets and autophagy in cancer: A nexus for therapeutic*
1032 *targeting.* Pharmacol Res, 2025. **222**: p. 108023.
1033 32. McDermott, M., et al., *In vitro Development of Chemotherapy and Targeted Therapy Drug-*
1034 *Resistant Cancer Cell Lines: A Practical Guide with Case Studies.* Front Oncol, 2014. **4**: p. 40.
1035 33. Adlimoghaddam, A., et al., *Sex and region-specific disruption of autophagy and mitophagy in*
1036 *Alzheimer's disease: linking cellular dysfunction to cognitive decline.* Cell Death Discov, 2025.
1037 **11**(1): p. 204.
1038 34. Alizadeh, J., et al., *Evaluation of Mitochondrial Phagy (Mitophagy) in Human Non-small*
1039 *Adenocarcinoma Tumor Cells.* Methods Mol Biol, 2025. **2879**: p. 261-273.
1040 35. Alizadeh, J., et al., *Mevalonate Cascade Inhibition by Simvastatin Induces the Intrinsic Apoptosis*
1041 *Pathway via Depletion of Isoprenoids in Tumor Cells.* Sci Rep, 2017. **7**: p. 44841.
1042 36. Shojaei, S., et al., *Simvastatin increases temozolomide-induced cell death by targeting the fusion*
1043 *of autophagosomes and lysosomes.* FEBS J, 2020. **287**(5): p. 1005-1034.
1044 37. Ghavami, S., et al., *Statin-triggered cell death in primary human lung mesenchymal cells involves*
1045 *p53-PUMA and release of Smac and Omi but not cytochrome c.* Biochim Biophys Acta, 2010.
1046 **1803**(4): p. 452-67.
1047 38. Folch, J., M. Lees, and G.H. Sloane Stanley, *A simple method for the isolation and purification of*
1048 *total lipides from animal tissues.* J Biol Chem, 1957. **226**(1): p. 497-509.
1049 39. Cole, L.K., R.L. Jacobs, and D.E. Vance, *Tamoxifen induces triacylglycerol accumulation in the*
1050 *mouse liver by activation of fatty acid synthesis.* Hepatology, 2010. **52**(4): p. 1258-65.
1051 40. Basso, J., et al., *Are we better together? Addressing a combined treatment of pitavastatin and*
1052 *temozolomide for brain cancer.* Eur J Pharmacol, 2024. **985**: p. 177087.
1053 41. Pirmoradi, L., et al., *Targeting cholesterol metabolism in glioblastoma: a new therapeutic*
1054 *approach in cancer therapy.* J Investig Med, 2019. **67**(4): p. 715-719.
1055 42. Shojaei, S., et al., *Unlocking a New Path: An Autophagometer that Measures Flux Using a Non-*
1056 *Fluorescent Immunohistochemistry Method.* bioRxiv, 2024.
1057 43. Ershov, P., et al., *Enzymes in the Cholesterol Synthesis Pathway: Interactomics in the Cancer*
1058 *Context.* Biomedicines, 2021. **9**(8).

1059 44. Juarez, D. and D.A. Fruman, *Targeting the Mevalonate Pathway in Cancer.* Trends Cancer, 2021.
1060 **7**(6): p. 525-540.
1061 45. Sethunath, V., et al., *Targeting the Mevalonate Pathway to Overcome Acquired Anti-HER2*
1062 *Treatment Resistance in Breast Cancer.* Mol Cancer Res, 2019. **17**(11): p. 2318-2330.
1063 46. Ghavami, S., et al., *Mevalonate cascade regulation of airway mesenchymal cell autophagy and*
1064 *apoptosis: a dual role for p53.* PLoS One, 2011. **6**(1): p. e16523.
1065 47. Toepfer, N., et al., *Atorvastatin induces autophagy in prostate cancer PC3 cells through activation*
1066 *of LC3 transcription.* Cancer Biol Ther, 2011. **12**(8): p. 691-9.
1067 48. Yang, Z., et al., *Fluvastatin Prevents Lung Adenocarcinoma Bone Metastasis by Triggering*
1068 *Autophagy.* EBioMedicine, 2017. **19**: p. 49-59.
1069 49. Bernhard, C., et al., *Glioblastoma Metabolism: Insights and Therapeutic Strategies.* Int J Mol Sci,
1070 2023. **24**(11).
1071 50. Davodabadi, F., et al., *Cancer chemotherapy resistance: Mechanisms and recent breakthrough in*
1072 *targeted drug delivery.* Eur J Pharmacol, 2023. **958**: p. 176013.
1073 51. Singh, R. and A.M. Cuervo, *Autophagy in the cellular energetic balance.* Cell Metab, 2011. **13**(5):
1074 p. 495-504.
1075 52. Dekker, L.J.M., et al., *Multiomics profiling of paired primary and recurrent glioblastoma patient*
1076 *tissues.* Neurooncol Adv, 2020. **2**(1): p. vdaa083.
1077 53. Liu, C., et al., *New insights into the therapeutic potentials of statins in cancer.* Front Pharmacol,
1078 2023. **14**: p. 1188926.
1079 54. Preta, G., *New Insights Into Targeting Membrane Lipids for Cancer Therapy.* Front Cell Dev Biol,
1080 2020. **8**: p. 571237.
1081 55. Hsu, T.I., *Editorial: Metabolic reprogramming for acquiring therapeutic resistance in glioblastoma.*
1082 Front Oncol, 2023. **13**: p. 1220063.
1083 56. Philipsen, M.H., et al., *Distinct Cholesterol Localization in Glioblastoma Multiforme Revealed by*
1084 *Mass Spectrometry Imaging.* ACS Chem Neurosci, 2023. **14**(9): p. 1602-1609.
1085 57. Shen, G., et al., *Autophagy as a target for glucocorticoid-induced osteoporosis therapy.* Cell Mol
1086 Life Sci, 2018. **75**(15): p. 2683-2693.
1087 58. Afzal, A., et al., *Functional role of autophagy in testicular and ovarian steroidogenesis.* Front Cell
1088 Dev Biol, 2024. **12**: p. 1384047.
1089 59. Ho, S.M., *Estrogen, progesterone and epithelial ovarian cancer.* Reprod Biol Endocrinol, 2003. **1**:
1090 p. 73.
1091 60. Menzies, F.M., et al., *Autophagy and Neurodegeneration: Pathogenic Mechanisms and*
1092 *Therapeutic Opportunities.* Neuron, 2017. **93**(5): p. 1015-1034.
1093 61. Sadeghi, A., et al., *Crosstalk between autophagy and insulin resistance: evidence from different*
1094 *tissues.* Eur J Med Res, 2023. **28**(1): p. 456.
1095 62. Jarocki, M., et al., *Lipids associated with autophagy: mechanisms and therapeutic targets.* Cell
1096 Death Discov, 2024. **10**(1): p. 460.
1097 63. Goldsmith, J., B. Levine, and J. Debnath, *Autophagy and cancer metabolism.* Methods Enzymol,
1098 2014. **542**: p. 25-57.
1099 64. Russell, R.C. and K.L. Guan, *The multifaceted role of autophagy in cancer.* The EMBO Journal, 2022.
1100 **41**(13): p. e110031.
1101 65. Debnath, J., N. Gammoh, and K.M. Ryan, *Autophagy and autophagy-related pathways in cancer.*
1102 Nat Rev Mol Cell Biol, 2023. **24**(8): p. 560-575.
1103 66. Xiao, M., et al., *Functional significance of cholesterol metabolism in cancer: from threat to*
1104 *treatment.* Exp Mol Med, 2023. **55**(9): p. 1982-1995.
1105 67. Xia, W., et al., *The role of cholesterol metabolism in tumor therapy, from bench to bed.* Front
1106 Pharmacol, 2023. **14**: p. 928821.

1107 68. Shapira, K.E., et al., *Autophagy is induced and modulated by cholesterol depletion through*
1108 *transcription of autophagy-related genes and attenuation of flux.* Cell Death Discov, 2021. **7**(1): p.
1109 320.
1110 69. Abdul Rashid, K., et al., *Lipid Alterations in Glioma: A Systematic Review.* Metabolites, 2022.
1111 **12**(12).
1112 70. Escamilla-Ramirez, A., et al., *Autophagy as a Potential Therapy for Malignant Glioma.*
1113 Pharmaceuticals (Basel), 2020. **13**(7).
1114 71. Thiery, J.P., et al., *Epithelial-mesenchymal transitions in development and disease.* Cell, 2009.
1115 **139**(5): p. 871-90.
1116 72. Tang, H., et al., *SRPX2 Enhances the Epithelial-Mesenchymal Transition and Temozolomide*
1117 *Resistance in Glioblastoma Cells.* Cell Mol Neurobiol, 2016. **36**(7): p. 1067-76.
1118 73. Zhao, J., *Cancer stem cells and chemoresistance: The smartest survives the raid.* Pharmacol Ther,
1119 2016. **160**: p. 145-58.
1120 74. Lindell, E., L. Zhong, and X. Zhang, *Quiescent Cancer Cells—A Potential Therapeutic Target to*
1121 *Overcome Tumor Resistance and Relapse.* International Journal of Molecular Sciences, 2023.
1122 **24**(4): p. 3762.
1123 75. Antonica, F., et al., *A slow-cycling/quiescent cells subpopulation is involved in glioma invasiveness.*
1124 Nat Commun, 2022. **13**(1): p. 4767.
1125 76. Brand, M.D. and D.G. Nicholls, *Assessing mitochondrial dysfunction in cells.* Biochem J, 2011.
1126 **435**(2): p. 297-312.
1127 77. Divakaruni, A.S. and M.D. Brand, *The regulation and physiology of mitochondrial proton leak.*
1128 Physiology (Bethesda), 2011. **26**(3): p. 192-205.
1129 78. Kimmelman, A.C., *The dynamic nature of autophagy in cancer.* Genes Dev, 2011. **25**(19): p. 1999-
1130 2010.
1131 79. Maharjan, Y., et al., *Intracellular cholesterol transport inhibition Impairs autophagy flux by*
1132 *decreasing autophagosome-lysosome fusion.* Cell Commun Signal, 2022. **20**(1): p. 189.
1133 80. Choo, M., et al., *Involvement of cell shape and lipid metabolism in glioblastoma resistance to*
1134 *temozolomide.* Acta Pharmacol Sin, 2023. **44**(3): p. 670-679.
1135 81. Tonkin-Reeves, A., C.M. Giuliani, and J.T. Price, *Inhibition of autophagy; an opportunity for the*
1136 *treatment of cancer resistance.* Front Cell Dev Biol, 2023. **11**: p. 1177440.
1137 82. Jusovic, M., et al., *The Combined Inhibition of Autophagy and Diacylglycerol Acyltransferase-*
1138 *Mediated Lipid Droplet Biogenesis Induces Cancer Cell Death during Acute Amino Acid Starvation.*
1139 Cancers (Basel), 2023. **15**(19).
1140 83. Yamamoto, Y., et al., *Involvement of Intracellular Cholesterol in Temozolomide-Induced*
1141 *Glioblastoma Cell Death.* Neurol Med Chir (Tokyo), 2018. **58**(7): p. 296-302.
1142 84. Alrosan, A.Z., et al., *The effects of statin therapy on brain tumors, particularly glioma: a review.*
1143 Anticancer Drugs, 2023. **34**(9): p. 985-994.
1144 85. Wu, H., et al., *Effect of simvastatin on glioma cell proliferation, migration, and apoptosis.*
1145 Neurosurgery, 2009. **65**(6): p. 1087-96; discussion 1096-7.
1146 86. Geng, F., et al., *Inhibition of SOAT1 Suppresses Glioblastoma Growth via Blocking SREBP-1-*
1147 *Mediated Lipogenesis.* Clin Cancer Res, 2016. **22**(21): p. 5337-5348.
1148 87. Bemlih, S., M.D. Poirier, and A. El Andaloussi, *Acyl-coenzyme A: cholesterol acyltransferase*
1149 *inhibitor Avasimibe affect survival and proliferation of glioma tumor cell lines.* Cancer Biol Ther,
1150 2010. **9**(12): p. 1025-32.
1151 88. Sun, T. and X. Xiao, *Targeting ACAT1 in cancer: from threat to treatment.* Frontiers in Oncology,
1152 2024. **14**.
1153 89. Ohmoto, T., et al., *K604, a specific acyl-CoA:cholesterol acyltransferase 1 inhibitor, suppresses*
1154 *proliferation of U251-MG glioblastoma cells.* Mol Med Rep, 2015. **12**(4): p. 6037-42.

1155 90. Tugnoli, V., et al., *Characterization of lipids from human brain tissues by multinuclear magnetic*
1156 *resonance spectroscopy.* Biopolymers, 2001. **62**(6): p. 297-306.
1157 91. Galluzzi, L. and D.R. Green, *Autophagy-Independent Functions of the Autophagy Machinery.* Cell,
1158 2019. **177**(7): p. 1682-1699.
1159 92. Laplante, M. and D.M. Sabatini, *mTOR signaling in growth control and disease.* Cell, 2012. **149**(2):
1160 p. 274-93.
1161 93. Cook, K.L. and R. Clarke, *Estrogen receptor-alpha signaling and localization regulates autophagy*
1162 *and unfolded protein response activation in ER+ breast cancer.* Receptors Clin Investig, 2014. **1**(6).
1163 94. Raut, P.K., et al., *Estrogen receptor signaling mediates leptin-induced growth of breast cancer cells*
1164 *via autophagy induction.* Oncotarget, 2017. **8**(65): p. 109417-109435.
1165 95. Sui, X., et al., *Autophagy and chemotherapy resistance: a promising therapeutic target for cancer*
1166 *treatment.* Cell Death Dis, 2013. **4**(10): p. e838.
1167 96. Sukumaran, P., et al., *Calcium Signaling Regulates Autophagy and Apoptosis.* Cells, 2021. **10**(8).
1168 97. Bootman, M.D., et al., *The regulation of autophagy by calcium signals: Do we have a consensus?*
1169 Cell Calcium, 2018. **70**: p. 32-46.
1170 98. Zhang, N., et al., *Autophagy regulates insulin resistance following endoplasmic reticulum stress in*
1171 *diabetes.* J Physiol Biochem, 2015. **71**(2): p. 319-27.
1172 99. Yang, Y., et al., *Interplay of CD36, autophagy, and lipid metabolism: insights into cancer*
1173 *progression.* Metabolism, 2024. **155**: p. 155905.
1174 100. Saito, T., et al., *Autophagy regulates lipid metabolism through selective turnover of NCoR1.* Nat
1175 Commun, 2019. **10**(1): p. 1567.

1176

Figure 1 A

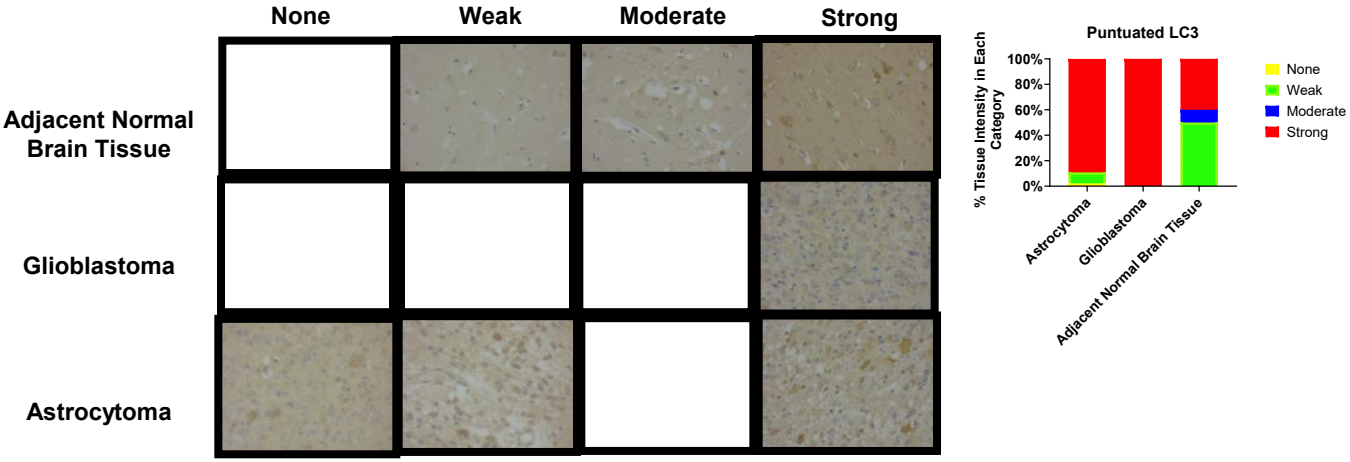
None
Weak
Moderate
Strong
Adjacent Normal Brain Tissue
Glioblastoma
Astrocytoma
Puntuated LC3
% Tissue Intensity in Each Category
100%
80%
60%
40%
20%
0%
Astrocytoma
Glioblastoma
Adjacent Normal Brain Tissue
None
Weak
Moderate
Strong

Figure 1 B

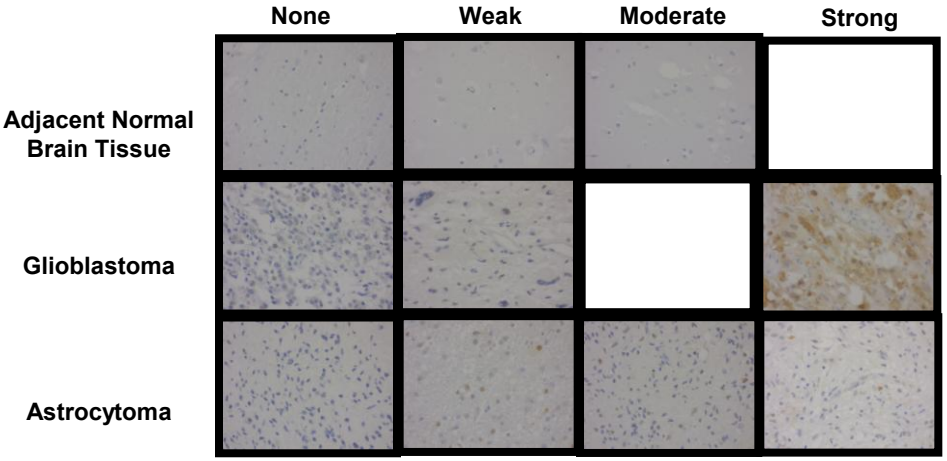
None
Weak
Moderate
Strong
Adjacent Normal Brain Tissue
Glioblastoma
Astrocytoma

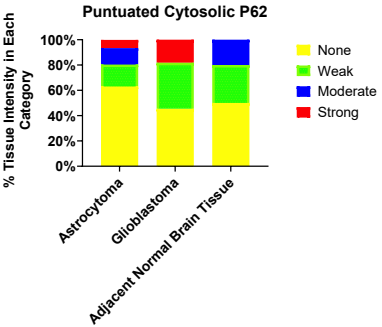
Puntuated Cytosolic P62
% Tissue Intensity in Each Category
100%
80%
60%
40%
20%
0%
Astrocytoma
Glioblastoma
Adjacent Normal Brain Tissue
None
Weak
Moderate
Strong

Figure 1 C

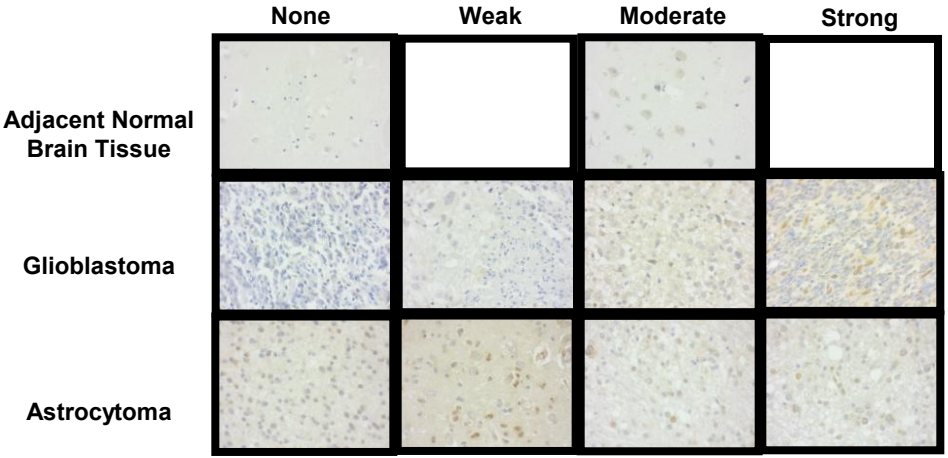
None
Weak
Moderate
Strong
Adjacent Normal Brain Tissue
Glioblastoma
Astrocytoma

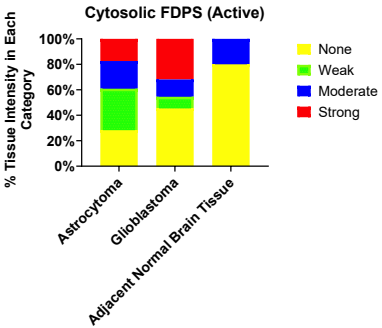
Cytosolic FDPS (Active)
% Tissue Intensity in Each Category
100%
80%
60%
40%
20%
0%
Astrocytoma
Glioblastoma
Adjacent Normal Brain Tissue
None
Weak
Moderate
Strong

Figure 1 D

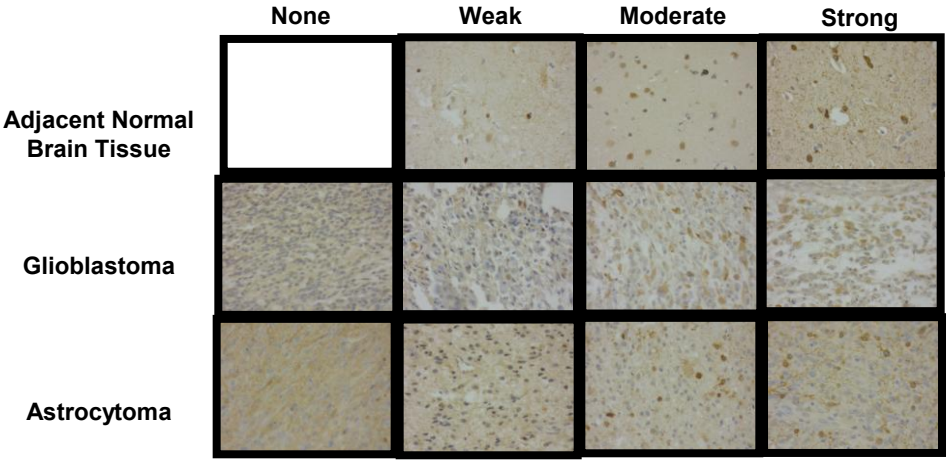
None
Weak
Moderate
Strong
Adjacent Normal Brain Tissue
Glioblastoma
Astrocytoma

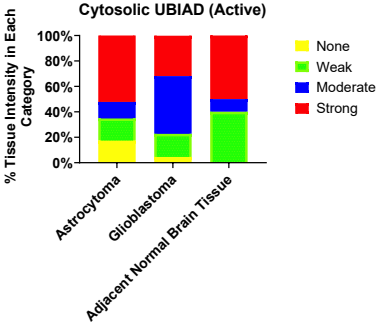
Cytosolic UBIAD (Active)
% Tissue Intensity in Each Category
100%
80%
60%
40%
20%
0%
Astrocytoma
Glioblastoma
Adjacent Normal Brain Tissue
None
Weak
Moderate
Strong

Figure 1 E

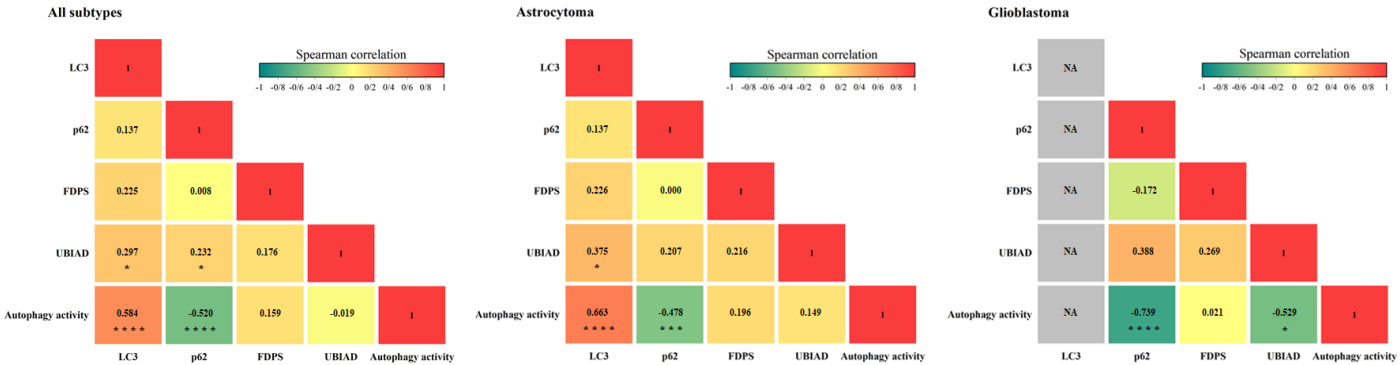
All subtypes
Spearman correlation
-1 -0/8 -0/6 -0/4 -0/2 0 0/2 0/4 0/6 0/8 1
LC3 1
p62 0.137 1
FDPS 0.225 0.008 1
UBIAD 0.297 * 0.232 * 0.176 1
Autophagy activity 0.584 * * * * -0.520 * * * * 0.159 -0.019 1
LC3 p62 FDPS UBIAD Autophagy activity
Astrocytoma
Spearman correlation
-1 -0/8 -0/6 -0/4 -0/2 0 0/2 0/4 0/6 0/8 1
LC3 1
p62 0.137 1
FDPS 0.226 0.000 1
UBIAD 0.375 * 0.207 0.216 1
Autophagy activity 0.663 * * * * -0.478 * * * 0.196 0.149 1
LC3 p62 FDPS UBIAD Autophagy activity
Glioblastoma
Spearman correlation
-1 -0/8 -0/6 -0/4 -0/2 0 0/2 0/4 0/6 0/8 1
LC3 NA
p62 NA 1
FDPS NA -0.172 1
UBIAD NA 0.388 0.269 1
Autophagy activity NA -0.739 * * * * 0.021 -0.529 * 1
LC3 p62 FDPS UBIAD Autophagy activity

Figure 2

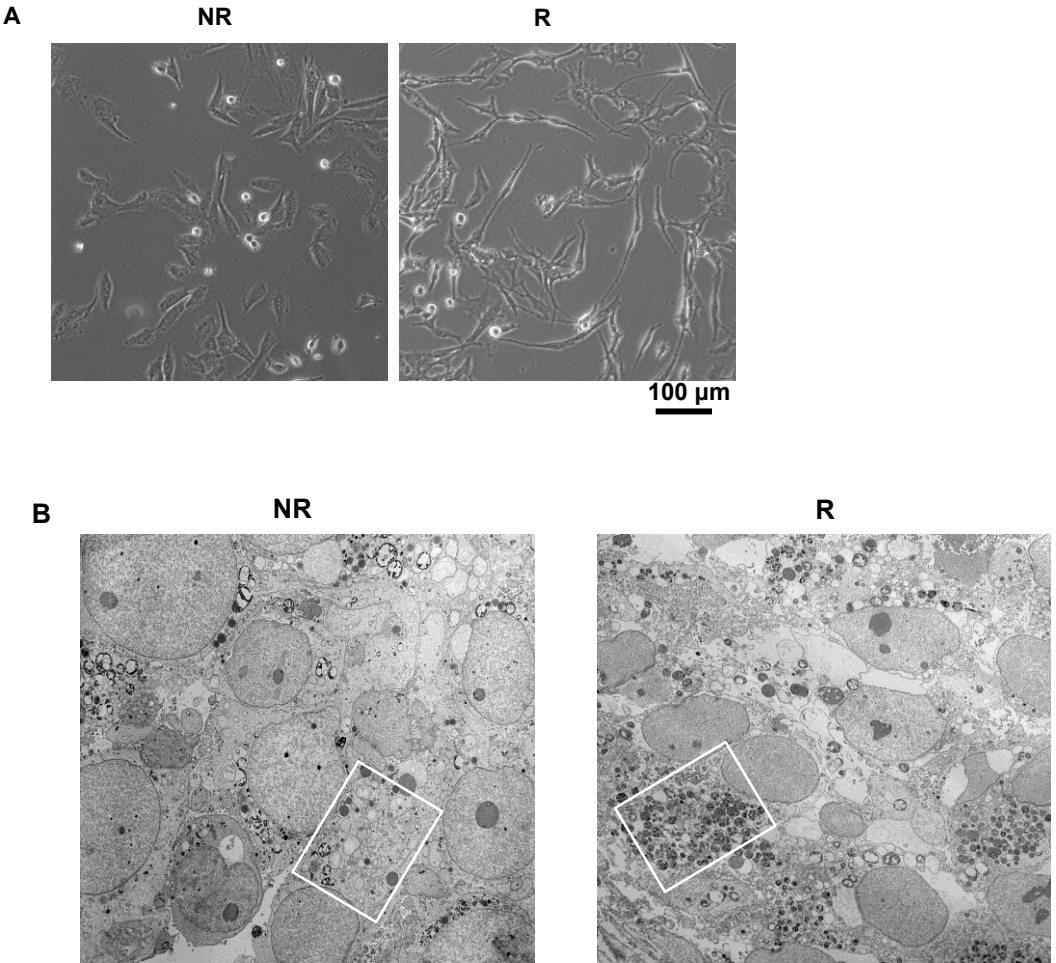

C

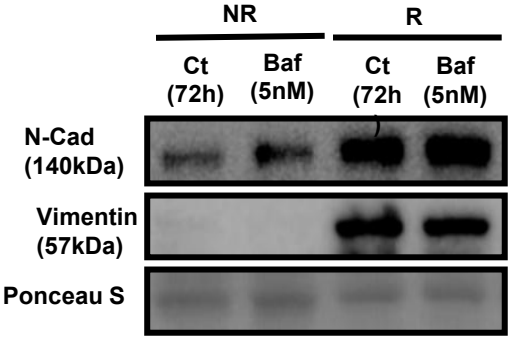
NR
R
Ct (72h)
Baf (5nM)
Ct (72h
Baf (5nM)
N-Cad (140kDa)
Vimentin (57kDa)
Ponceau S

D

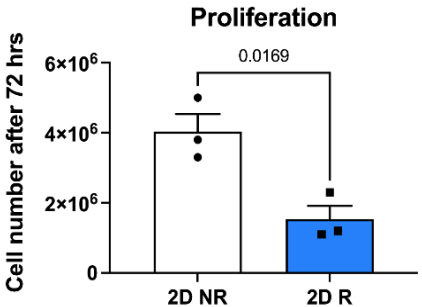
Proliferation
Cell number after 72 hrs
6×10^6
4×10^6
2×10^6
0
0.0169
2D NR
2D R

E

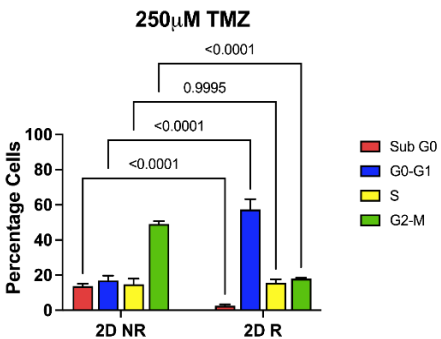
250μM TMZ
Percentage Cells
100
80
60
40
20
0
<0.0001
0.9995
<0.0001
<0.0001
2D NR
2D R
Sub G0
G0-G1
S
G2-M

Figure 2

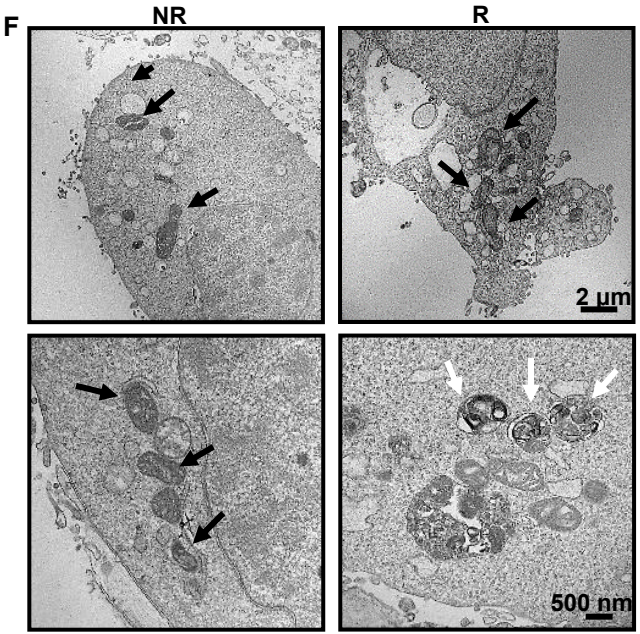

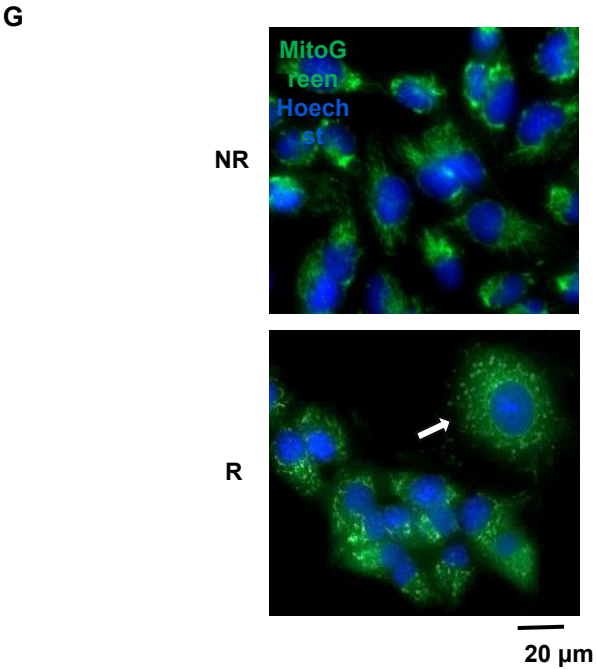

Figure 2

H

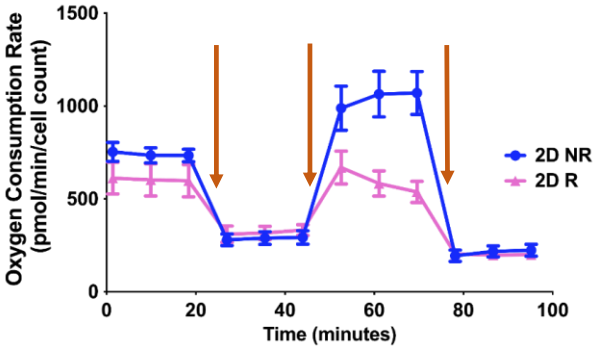
Oxygen Consumption Rate
(pmol/min/cell count)
1500
1000
500
0
0
20
40
60
80
100
Time (minutes)
2D NR
2D R

I

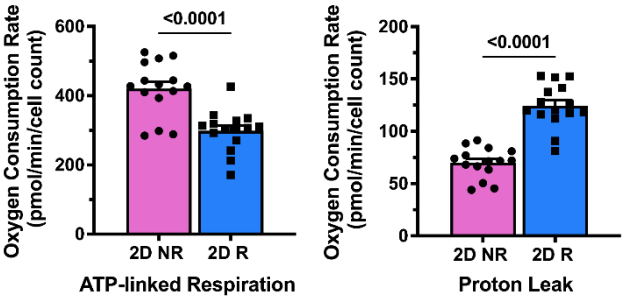
Oxygen Consumption Rate
(pmol/min/cell count)
600
400
200
0
<0.0001
2D NR
2D R
ATP-linked Respiration
Oxygen Consumption Rate
(pmol/min/cell count)
200
150
100
50
0
<0.0001
2D NR
2D R
Proton Leak

Figure 3

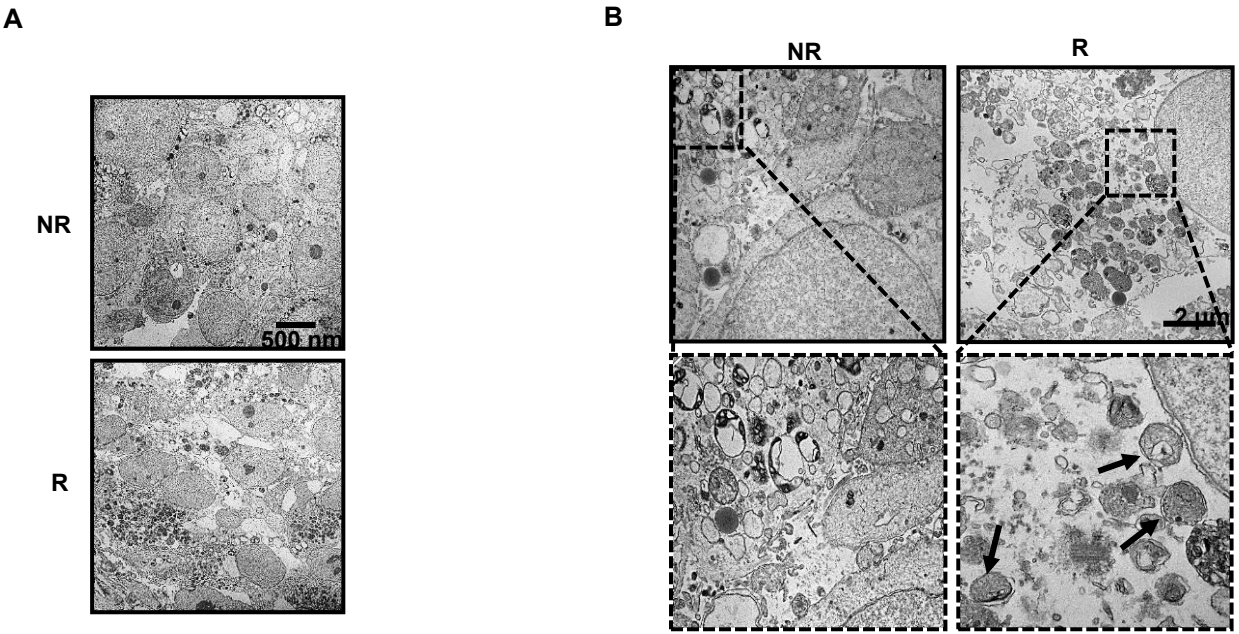

Figure 3

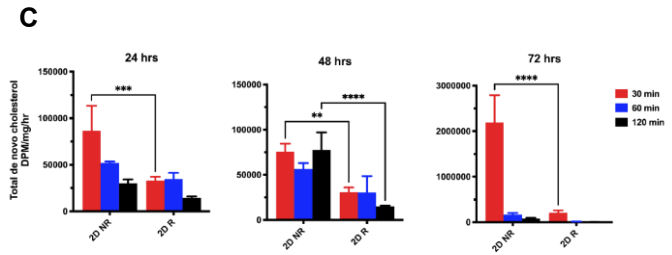
C
24 hrs
48 hrs
72 hrs
Total de novo cholesterol DPM/mg/hr
150000
100000
50000
0
3000000
2000000
1000000
***
**
****
2D NR
2D R
30 min
60 min
120 min

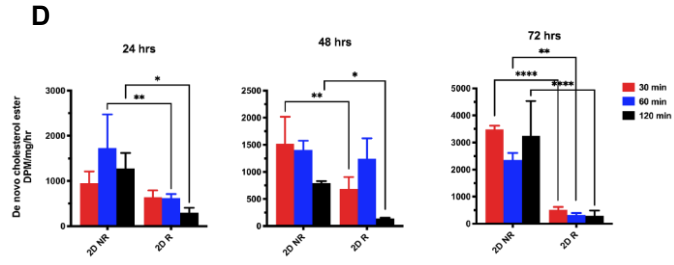
D
24 hrs
48 hrs
72 hrs
De novo cholesterol ester DPM/mg/hr
3000
2000
1000
0
2500
1500
500
5000
4000
3000
*
**
****
2D NR
2D R
30 min
60 min
120 min

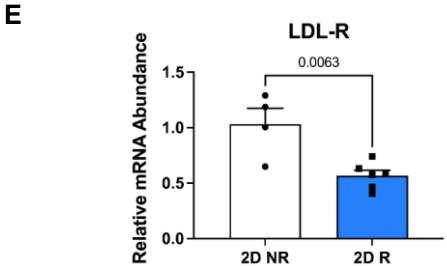
E
LDL-R
0.0063
Relative mRNA Abundance
1.5
1.0
0.5
0.0
2D NR
2D R

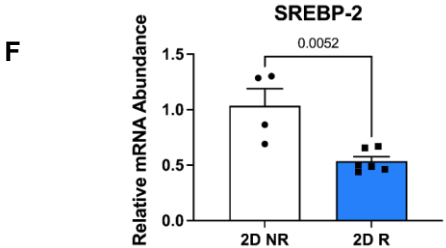
F
SREBP-2
0.0052
Relative mRNA Abundance
1.5
1.0
0.5
0.0
2D NR
2D R

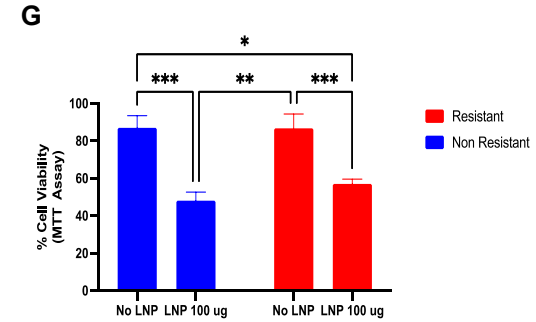
G
*
***
**
***
% Cell Viability (MTT Assay)
100
80
60
40
20
0
No LNP
LNP 100 ug
No LNP
LNP 100 ug
Resistant
Non Resistant

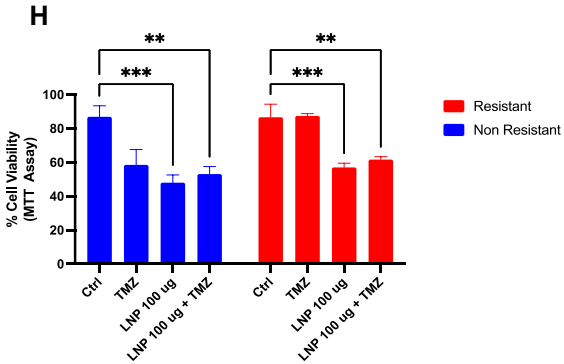
H
**
***
**
***
% Cell Viability (MTT Assay)
100
80
60
40
20
0
Ctrl
TMZ
LNP 100 ug
LNP 100 ug + TMZ
Ctrl
TMZ
LNP 100 ug
LNP 100 ug + TMZ
Resistant
Non Resistant

Figure 4

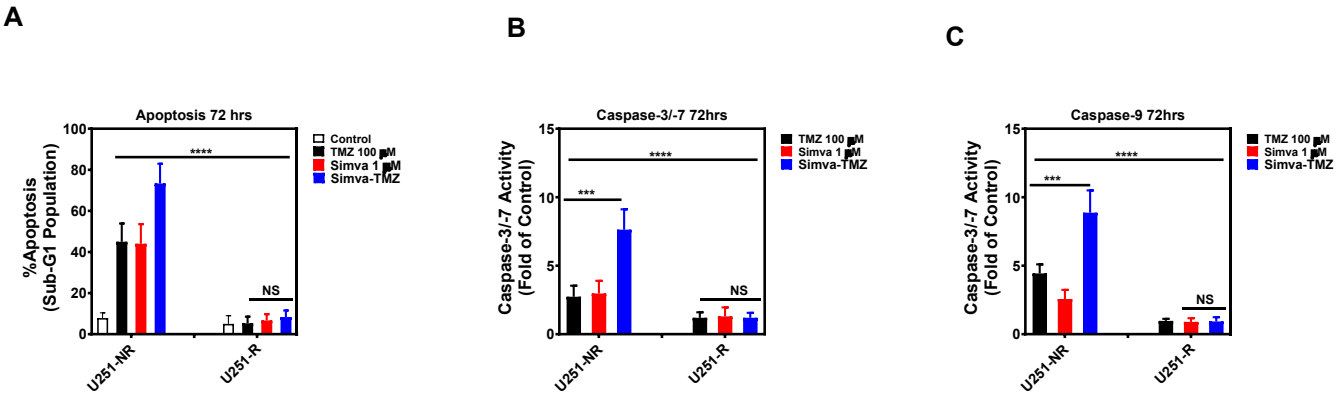
A
Apoptosis 72 hrs
%Apoptosis
(Sub-G1 Population)
100
80
60
40
20
0
****
NS
Control
TMZ 100 μM
Simva 1 μM
Simva-TMZ
U251-NR
U251-R
B
Caspase-3/-7 72hrs
Caspase-3/-7 Activity
(Fold of Control)
15
10
5
0
****
***
NS
TMZ 100 μM
Simva 1 μM
Simva-TMZ
U251-NR
U251-R
C
Caspase-9 72hrs
Caspase-3/-7 Activity
(Fold of Control)
15
10
5
0
****
***
NS
TMZ 100 μM
Simva 1 μM
Simva-TMZ
U251-NR
U251-R

Figure 5

A

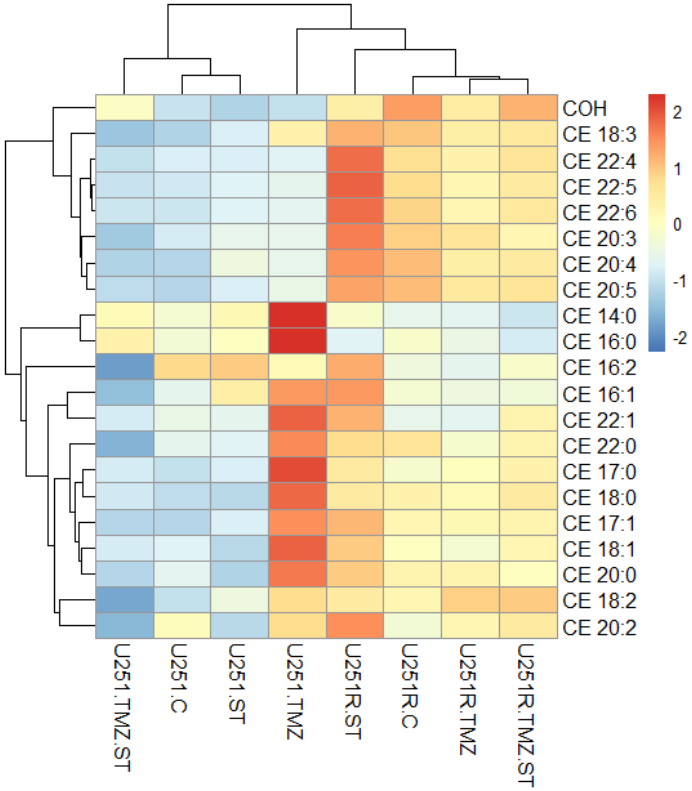
COH
CE 18:3
CE 22:4
CE 22:5
CE 22:6
CE 20:3
CE 20:4
CE 20:5
CE 14:0
CE 16:0
CE 16:2
CE 16:1
CE 22:1
CE 22:0
CE 17:0
CE 18:0
CE 17:1
CE 18:1
CE 20:0
CE 18:2
CE 20:2
U251.TMZ.ST
U251.C
U251.ST
U251.TMZ
U251R.ST
U251R.C
U251R.TMZ
U251R.TMZ.ST
2
1
0
-1
-2

B

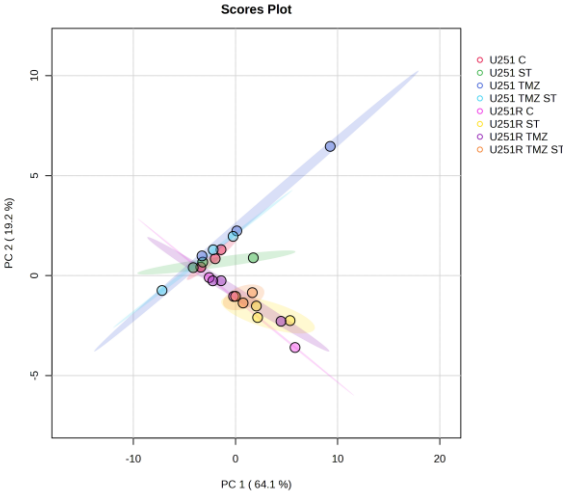
Scores Plot
U251 C
U251 ST
U251 TMZ
U251 TMZ ST
U251R C
U251R ST
U251R TMZ
U251R TMZ ST
PC 2 (19.2 %)
PC 1 (64.1 %)
-10
0
10
20
-5
0
5
10

Figure 5

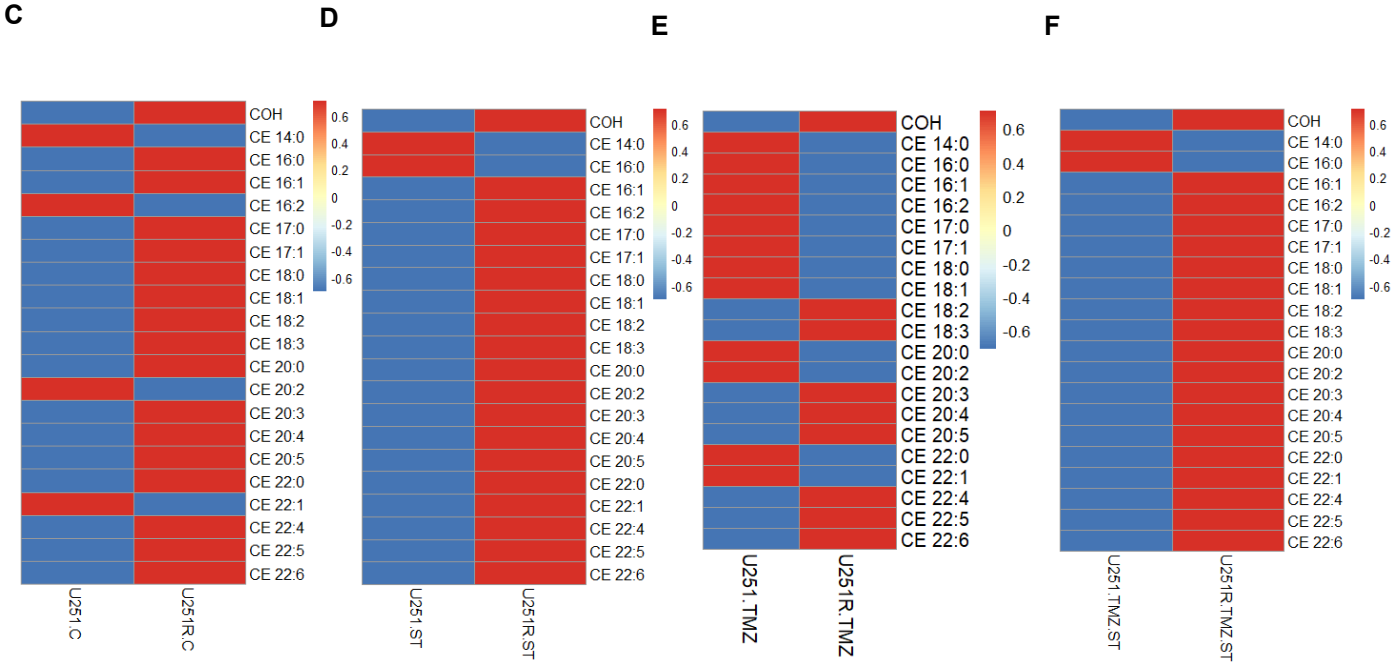
C
D
E
F
COH
CE 14:0
CE 16:0
CE 16:1
CE 16:2
CE 17:0
CE 17:1
CE 18:0
CE 18:1
CE 18:2
CE 18:3
CE 20:0
CE 20:2
CE 20:3
CE 20:4
CE 20:5
CE 22:0
CE 22:1
CE 22:4
CE 22:5
CE 22:6
0.6
0.4
0.2
0
-0.2
-0.4
-0.6
U251.C
U251R.C
U251.ST
U251R.ST
U251.TMZ
U251R.TMZ
U251.TMZ.ST
U251R.TMZ.ST

Figure 5

G

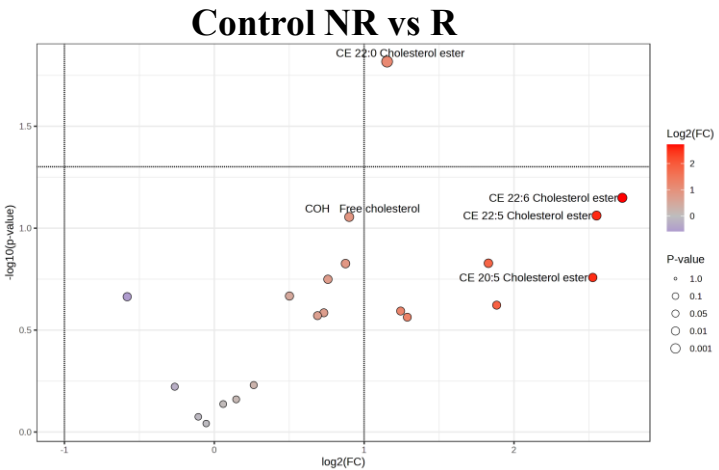
Control NR vs R
CE 22:0 Cholesterol ester
COH Free cholesterol
CE 22:6 Cholesterol ester
CE 22:5 Cholesterol ester
CE 20:5 Cholesterol ester
-log10(p-value)
log2(FC)
Log2(FC)
P-value
1.0
0.1
0.05
0.01
0.001

H

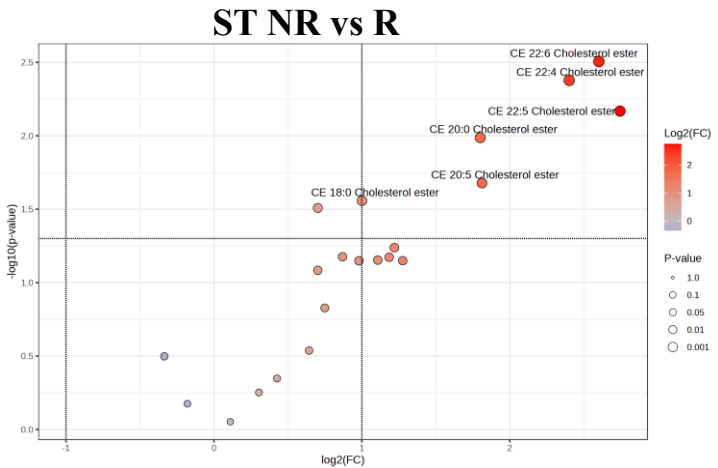
ST NR vs R
CE 22:6 Cholesterol ester
CE 22:4 Cholesterol ester
CE 22:5 Cholesterol ester
CE 20:0 Cholesterol ester
CE 20:5 Cholesterol ester
CE 18:0 Cholesterol ester
-log10(p-value)
log2(FC)
Log2(FC)
P-value
1.0
0.1
0.05
0.01
0.001

I

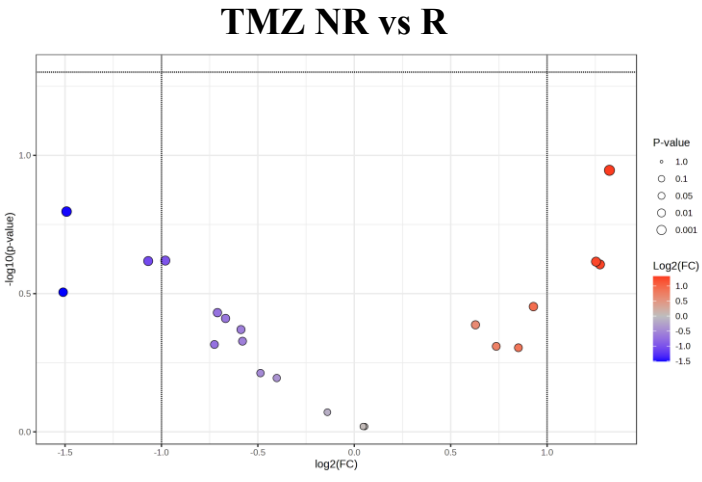
TMZ NR vs R
-log10(p-value)
log2(FC)
P-value
1.0
0.1
0.05
0.01
0.001
Log2(FC)
1.0
0.5
0.0
-0.5
-1.0
-1.5

J

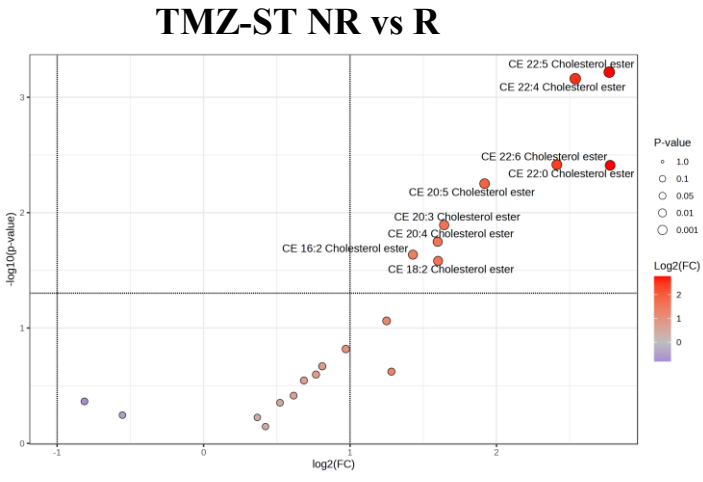
TMZ-ST NR vs R
CE 22:5 Cholesterol ester
CE 22:4 Cholesterol ester
CE 22:6 Cholesterol ester
CE 22:0 Cholesterol ester
CE 20:5 Cholesterol ester
CE 20:3 Cholesterol ester
CE 20:4 Cholesterol ester
CE 16:2 Cholesterol ester
CE 18:2 Cholesterol ester
-log10(p-value)
log2(FC)
P-value
1.0
0.1
0.05
0.01
0.001
Log2(FC)
2
1
0

Figure 5

K

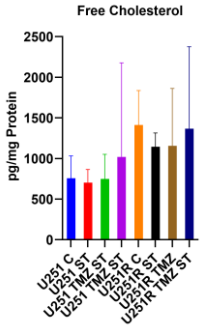

L

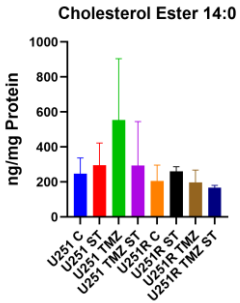

M

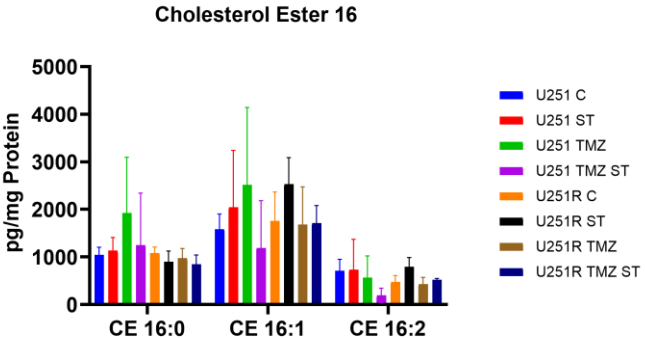

N

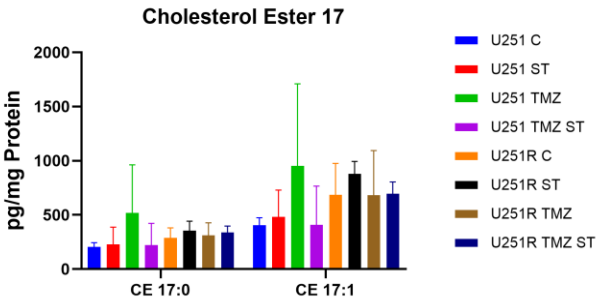

O

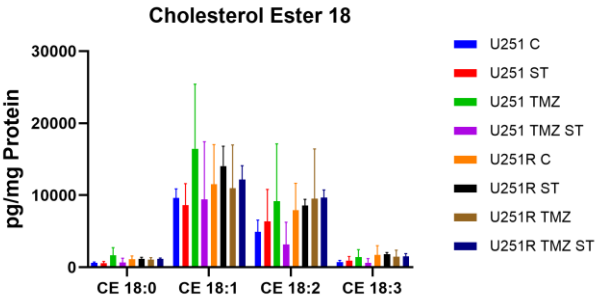

Figure 5

P

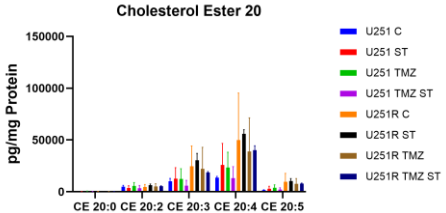

Q

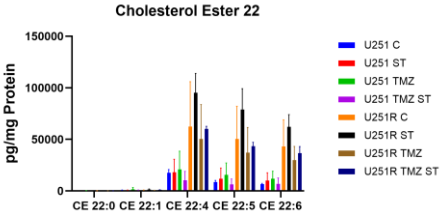

R

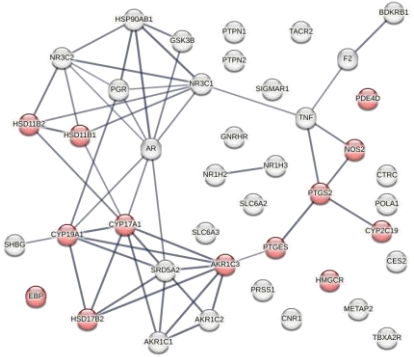

S

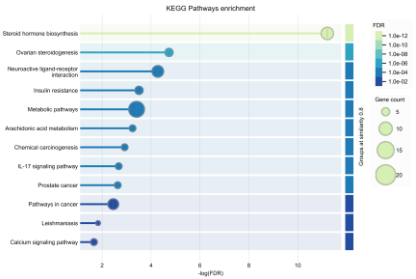

Figure 6

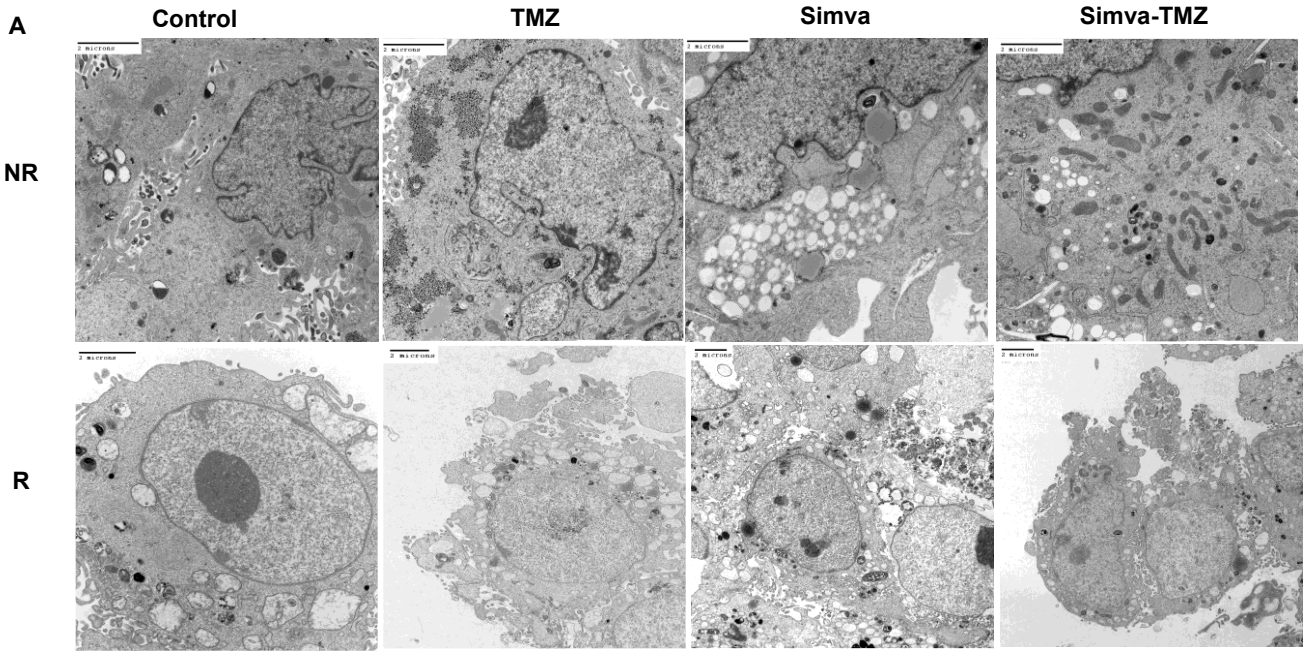

Figure 6

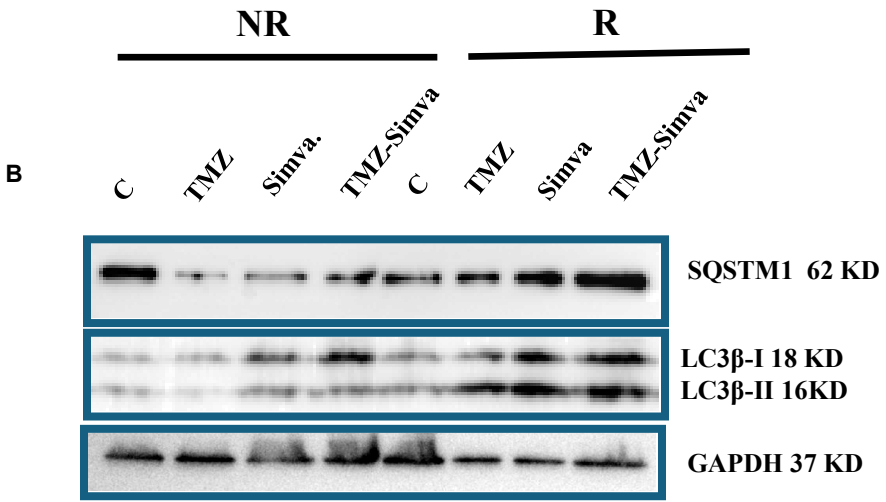
NR
R
B
C
TMZ
Simva.
TMZ-Simva
C
TMZ
Simva
TMZ-Simva
SQSTM1 62 KD
LC3β-I 18 KD
LC3β-II 16KD
GAPDH 37 KD